COMPUTATIONAL MODELING AND SIMULATION FOR PROJECTILE IMPACT AND INDENTATION OF BIOLOGICAL TISSUES AND POLYMERS

by

Kyle Geiser

MASSACHUSETTS INSTITUTE OF TECHNOLOGY

Submitted to the Department of Biological Engineering in partial
fulfilment of the requirements for the degree of
MASTERS OF SCIENCE IN BIOLOGICAL ENGINEERING

May 2017 [June 2017]

Signature of Author:____ Signature redacted _____
Department of Biological Engineering
May 26, 2017

Certified by:_____ Signature redacted _____
Krystyn J. Van Vliet
Professor of Material Science and Engineering and Biological Engineering
Thesis Supervisor

Accepted by:_____ Signature redacted _____
Mark Bathe
Professor of Biological Engineering
Chair, Course XX Committee for Graduate Students

Computational Modeling and Simulation for Projectile Impact and Indentation of Biological Tissues and Polymers

By

Kyle Geiser

Submitted to the Department of Biological Engineering

on May 26, 2007 in Partial Fulfilment of the

Requirements for the Degree of Master of Science in

Biological Engineering

ABSTRACT

Understanding the elastic and viscoelastic responses of biological soft tissues and engineered polymer simulants is of great interest to predicting and preventing penetrative injuries. Detailed understanding of the mechanical processes at work could aid in the development and evaluation of protective strategies such as armor and helmets, and repair strategies including robotic surgery or needle-based drug delivery. However, due to the mechanical complexity of so-called "soft tissues," including nonlinear viscoelastic behavior, surface adhesion, material failures and shock effects, the experimental characterization of various soft tissues is challenging and individual mechanical processes are often impossible to decouple without computational models and simulations.

This thesis presents two finite element models designed to provide both replicate the results of indentation and impact experiments on synthetic polymers, aimed to decouple competing mechanical characteristics of contact based deformation. The first of these models describes the indentation on polydimethylsiloxane bilayer composites, with the aim of describing the relative effects of a adhesion and viscoelastic properties on the measured deformation response. That model expands on this objective via the analysis of the effects of surface adhesion commonly associated with highly compliant polymers and tissues. The second model attempts to replicate impact of a high velocity projectile on a relatively stiff material, polyurethane urea, and on a comparatively compliant polymer, gelatin hydrogel. These models provide means to simulate, predict and characterize material response, validated by comparison with available experiments. Such validated models can be used to simulate and design new materials as tissue simulants or as protective media that predictably dissipate concentrated mechanical impact.

Thesis Supervisor: Krystyn J. Van Vliet

Title: Professor of Material Science and Engineering and Biological Engineering

ACKNOWLEDGEMENTS

I would first like to thank my advisor, Professor Krystyn Van Vliet, whose near infinite patience and direction made this work possible, and my DRAPER supervisor, Dr. Jefferey Borenstein, for his commitment and support during this long process. I'd also like to thank my group mates, especially Bo Qing and Alexander Mijailovic for their help in the design, testing and experimentation done in this thesis. Finally, I'd like to thank my family and my friends especially, Claire, Caleigh, Adam, Mary, Tarek, Ehab, Jay, Alex and Jess. Without you all, I would not have been able to complete this thesis.

CONTENTS

1 Introduction **11**

1.1 MOTIVATION 12

1.1.1 Modeling Impact on Soft Tissues 13

1.1.2 Current Polymers Considered as Tissue Simulants for Impact 14

1.2 MECHANICAL MODELS OF COMPLIANT TISSUES 17

1.2.1 Elastic Models 17

1.2.2 Viscoelastic Models 18

1.2.3 Hyperelastic Models 21

1.2.4 Effects of Shock loading 21

1.2.5 Material Failure 25

1.2.6 Effects of Adhesion 28

1.3 THESIS ORGANIZATION 32

2 Indentation Modelling **33**

2.1 INTRODUCTION 33

2.1.1 Sample Preperation 33

2.1.2 Viscoelastic Response Investigation 33

2.1.3 Experimental Setup 37

2.2 FINITE ELEMENT MODELLING 38

2.2.1 Representative Volume Elements 39

2.2.2 The Finite Element Model 40

2.2.3 Viscoelastic Experimental Results 43

2.2.4 Implementing Adhesion 45

2.3 INVESTIGATING ADHESION 49

2.3.1 Strength of Adhesion 50

2.3.2 The Effect of Strain Rate on Adhesive Response 52

2.3.3 Quantifying Hysteresis as a Function of the Strength of Adhesion 54

2.3.4 Decoupling Adhesion from Viscous Response 58

2.3.4 Limits of the Model 61

3 Impact Modelling 63

3.1 POLY(URETHANE UREA) CASE STUDY 64

3.1.1 Poly(urethane urea) Microstructure and Properties 64

3.1.2 Calculated Materials Properties 66

3.1.3 Derived Shock Data 67

3.1.4 Experimental Setup 71

3.1.5 Finite Element Model Setup 72

3.1.6 Model Comparison 74

3.1.7 Model Expansion (Polycarbonate) 76

3.2 GELATIN CASE STUDY 78

3.2.1 Gelatin Microstructure and Properties 78

3.2.2 Literature Materials Properties 78

3.2.3 Finite Element Model Setup 79

3.2.4 Model Comparison 81

3.3 MODEL LIMITATIONS 84

4 Summary and Future Work 86

5 References 89

6 Appendices 96

6.1.1 Matlab Code For Rheology Data 97

6.2 Model Sample Input Files 100

6.3 Example Output Files 100

6.4 Archived List of Models and Locations of Stored Data 100

6.5 Sample Calculation of Interfacial Energy γ_{12} from Traction Stress 101

6.6 Comparison of FEM Particle impact simulation with Analytical Models 103

LIST OF TABLES

TABLE 2.1: RELATIVE MODULI AND RESPECTIVE RELAXATION TIMES OF COMMERCIAL PDMS (CY52) 38

TABLE 2.2: COMPARISON OF DISSIPATED WORK AND STRAIN RATE AT VARIABLE TRACTION STRESS 62

TABLE 3.1: DISTINCT UNLOADING STATES OF SODA LIME GLASS AT 298 M/S 70

TABLE 3.2: LITERATURE VALUES FOR GELATIN MATERIAL PROPERTIES 79

TABLE 6.1.1: PRONY SERIES COMPONENTS OF CY52 USED IN CHP2 97

LIST OF FIGURES

FIGURE 1-1. RESEARCH MOTIVATION AND PROCESS: 14

FIGURE 1-2. CHAIN ENTANGLE EVENT IN GELATIN HYDROGELS: 16

FIGURE 1-3. STRUCTURE OF PDMS GELS: 17

FIGURE 1-4. MAXWELL MODEL OF VISCOELASTIC RESPONSE: 19

FIGURE 1-5. VOIGT MODEL OF VISCOELASTIC RESPONSE: 20

FIGURE 1-6. GENERALIZED MAXWELL MODEL: 21

FIGURE 1-7. EFFECTS OF SHOCK: 23

FIGURE 1-8. SHOCK EQUATION OF STATE: 24

FIGURE 1-9. SHOCK HUGONIOT: 25

FIGURE 1-10. SLIDING FRICTIONAL ELEMENT: 27

FIGURE 1-11. ELASTOVISCOPLASTIC STRESS RESPONSE: 28

FIGURE 1-12. PERFECTLY ELASTIC VERSUS ADHESIVE: 30

FIGURE 2-1. SHEAR RHEOLOGY SETUP AND PHASE LAG DETERMINATION: 35

FIGURE 2-2. RHEOLOGY OF CY52: 37

FIGURE 2-3. RHEOLOGY OF SURFACE COATING: 37

FIGURE 2-4. EXPERIMENTAL SETUP: 39

FIGURE 2-5. RVE MESH AND SIZING: 41

FIGURE 2-6. MODEL SETUP: 42

FIGURE 2-7. MESH CONVERGENCE STUDY: 43

FIGURE 2-8. DISPLACEMENT CONTROLLED PROFILE: 44

FIGURE 2-9. INDENTATION EXPERIMENT AND MODEL COMPARISON: 45

FIGURE 2-10. WORKBENCH FILE ARCHITECTURE: 46

FIGURE 2-11. FRACTURE ENERGIES BASED DE-BONDING: 48

FIGURE 2-12. MODIFICATION OF CONTACT: 48

FIGURE 2-13. TRANSIENT CONTROL SYSTEM: 49

FIGURE 2-14. NON-ADHESIVE VERSUS ADHESIVE RESPONSE: 50

FIGURE 2-15. EFFECT OF ADHESIVE STRENGTH: 51

FIGURE 2-16. CONTACT AREA COMPARISON: 52

FIGURE 2-17. COMPARISON BETWEEN FLAT PUNCH AND SPHERICAL INDENTER: 53

FIGURE 2-18. EFFECT OF PROBE DISPLACEMENT RATE ON REACTION FORCE: 54

FIGURE 2-19. EFFECT OF PROBE DISPLACEMENT RATE ON REACTION AND PULL OFF FORCE: 55

FIGURE 2-20. LOAD-DEPTH HYSTERESIS OF INDENTATION: 56

FIGURE 2-21. COMPARISON OF DISSIPATED WORK OF INDENTATION: 57

FIGURE 2-22. WORK OF SEPARATION: 57

FIGURE 2-23. INTERFACIAL ENERGY COMPARISON: 58

FIGURE 2-24. FORCE-DISPLACEMENT PROFILE AT A PROBE DISPLACEMENT RATE OF 16MM/S: 59

FIGURE 2-25. SELECT COMPARISON BETWEEN PROBE DISPLACEMENT RATE RESPONSES WITHOUT ADHESION: 60

FIGURE 2-26. DISSIPATED WORK OF INDENTATION COMPARISON: 61

FIGURE 3-1. PUU FORMULATION: 66

FIGURE 3-2. SLG TEST SETUP: 69

FIGURE 3-3. SLG VISAR RESPONSE AT 298M/S IMPACT: 70

FIGURE 3-4. STRESS VS STRAIN FOR DISTINCT UNLOADING STATES: 71

FIGURE 3-5. PARTICLE SPEED VERSUS SHOCK SPEED OF PUU 532-1000: 71

FIGURE 3-6. PARTICLE LAUNCH AND IMAGING CONFIGURATION: 73

FIGURE 3-7. FINITE ELEMENT MODEL SETUP: 74

FIGURE 3-8. MESH CONVERGENCE STUDY FOR PUU AT 500M/S: 75

FIGURE 3-9. IMPACT PROFILE COMPARISON: 75

FIGURE 3-10. COEFFICIENT OF RESTITUTION COMPARISON: 76

FIGURE 3-11. TEMPERATURE/IMPACT STUDY OF PUU 532-1000: 77

FIGURE 3-12. COMPARISON OF SHOCK ENABLED AND SHOCK DISABLED MODELS: 78

FIGURE 3-13. GELATIN IMPACT MODEL: 81

FIGURE 3-14. MESH CONVERGENCE STUDY: 82

FIGURE 3-15. EXPERIMENTAL VERSUS FEM MODEL COMPARISON: 83

FIGURE 3-16. IMPACT PROFILE: 84

FIGURE 6-1. COMPARISON OF 10% GELATIN, FITTED PONCELET MODEL FROM D. VEYSSET AND FEM MODEL OF THE AUTHOR: 103

1 INTRODUCTION

1.1 Motivation

Measuring and decoupling the mechanical responses of soft tissues is of interest for both the investigation of the effects of disease, and for the understanding of blunt and penetrative trauma common in high stress environments like military operations. Indeed, the majority of combat related injuries stems from high velocity impacts, while the majority of noncombat related injuries stems from blunt force trauma. The prevalence of projectile impact injury necessitates development of mechanical models of so-called "soft tissues" that cover a diverse spectrum of impact speed and characteristics.[1] Here quotes are used to note that tissues from organs such as heart, liver and brain are not mechanically soft, as defined by low resistance to permanent or plastic deformation, but are referred to in the medical and general community with this term. In fact, such tissues are mechanically compliant, meaning they exhibit a low elastic modulus relative to stiffer tissues. In this thesis, we present and examine two finite element models that can viably investigate and predict the response of soft tissue and compliant polymer simulants under diverse impact velocities. Figure 1.1 describes motivation for research done within this thesis.

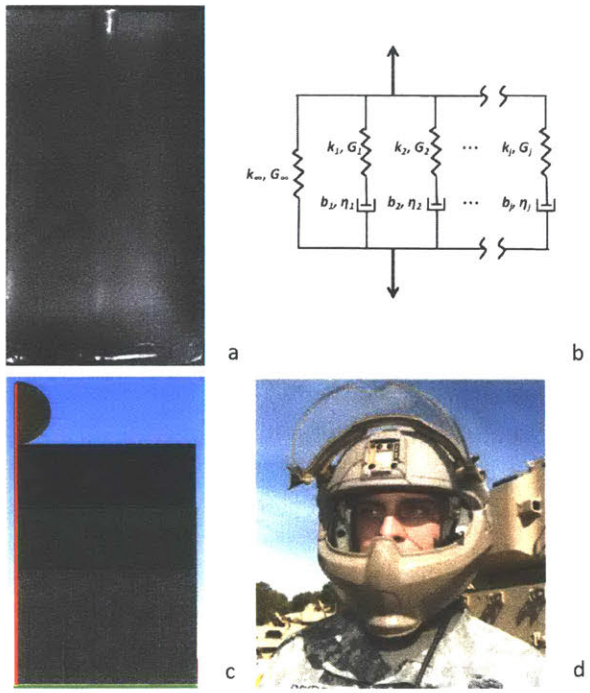

Figure 1-1. Research Motivation and Process: (a) Experimental capture of not fully understood and characterized mechanical processes (From Wen et al.) (b) Assignment of constitutive laws and governing equations (From Mijailovic et al.[2]) (c) Conversion of constitutive laws to finite element models for testing and analysis. (d) Use refined model analysis to aid in the testing and development of new protective systems for soldiers and civilians alike (from Department of the Army.[3])

1.1.1 Modelling Impact on Soft Tissues

Modelling impact related to soft tissue injury and response is well known to be complicated by myriad confounding variables. Since live human testing is not feasible or practical, the closest related models historically were human cadaver and animal models, each with its own set of complications. Human cadaver models only costly and potentially risk the spread of communicable disease, and also do not maintain the structure, hydration, and mechanical properties of live tissues to validate testing.[1-4] Further, the average age of cadaver specimens is seventy-two years old, (with eighty percent of cadavers obtained between the ages of seventy and eighty years old).[5] Since many injuries of interest can occur for humans at younger ages for most combat or sports related contexts, this may also invalidate or skew mechanical data obtained from such tests.

Animals models, primarily porcine (pig) and bovine (cow) have long been used in place of human models for practical and economic reasons. Many tissues, such as those of skin and some internal organs (including the kidneys, heart and lungs), have been shown to replicate the shape and trend of human cadaver responses, if not the actual quantitative response of those tissues.[6] However, animal models introduce additional confounding factors, including the composition and stiffness of internal tissues, the thickness of bone and connective tissues, and differences in anatomical structure and layout of internal features.[7] Despite the usefulness of both human and animal tissue models, they also suffer from another considerable hindrance to mechanical study in that the tissues themselves are opaque and thus difficult to analyse at non-bulk levels and low timescales. Instead, what is needed to effectively model impact and indentation on the many different tissues of the human anatomy are consistent, tunable materials capable of replicating the complex mechanical responses while also representing significantly reduced costs and health hazards associated with human cadaver and animal models. Such materials exist in the form of synthetic and biological polymers.

1.1.2 Current Polymers Considered as Tissue Simulants for Impact Response

In part because of the complex nature of organs and tissues, numerous synthetic and biological polymers and hydrogels have been employed to simulate tissues of the human body including adipose,[8] ballistic soap,[9] polyethylene,[10] polyester resin, polystyrene, polyurethane and polyisoprene,[11] methacryloyl,[7] and silicone.[12] However, by far the most common material used to simulate tissues of the human body are hydrogel formulations of gelatin. Gelatin is a term for denatured collagen, and is formed via partial acidic hydrolysis of collagen derived from skin, bone and connective tissue of various animals. The addition of water causes the formation of a transparent hydrogel whose elastic and viscoelastic mechanical properties are tunable based on the percentage by weight of the added gelatin.[13] The tunability of gelatin is a result of order of

chain entanglements brought about by the concentration of collagen within the block detailed in Figure 1.2 below:

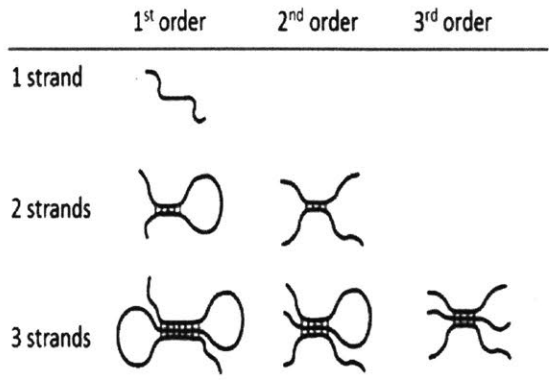

Figure 1-2. Chain entangle event in gelatin hydrogels: Increasing complexity of chain interactions occurs as the concentration of denatured collagen within the gel increases. As the percent weight of gelatin increases, there are likely to be more crosslinks between chains, resulting in a stiffer response from the material (from Duconseille et al.)[14]

Though highly versatile, inexpensive, and widely used in studies of bullet trajectory, depth of penetration, analysis of temporary and permanent wound cavities, and bullet fragmentation,[11] gelatin does have certain drawbacks that researchers should be aware of when employing the material. Gelatin lacks consistent viscoelastic responses owing to variability in the forming process, has short shelf-life measured in hours, and suffers from structural degradation under prolonged usage at room temperature.[11] Further, gelatin, even at some of its lowest percent formulations, is more than an order of magnitude stiffer than some of the most compliant tissues of the body, namely brain tissue.[15] These drawbacks, coupled with the potential inhomogeneity of the gel, make this biological polymer hydrogel questionable for quantitative mimicry of tissue mechanics, but adequate for some types of qualitative work. An alternative material for study that offers many of the tunable advantages of gelatin with fewer materials-related drawbacks is a synthetic polymer termed polydimethylsiloxane (PDMS).

PDMS is a physically and chemically stable silicone rubber, formed via a crosslinking process involving variable ratios of vinyl terminated PDMS (v-PDMS) and tetrafunctional

tetrakis (dimethyl siloxy)silane crosslinker in the presence of a platinum catalyst.[16] The silane crosslinker caps the v-PDMS with methyl groups (shown in Figure 1.3 below), resulting in an inert non-reactive chain (m-PDMS). The result of the reaction is a networked, coherent, solid for which elastic and viscoelastic properties are dependent on the degree of crosslinking imposed during the forming process. Indeed, recent work from the U.S. Army Research Laboratory and the Van Vliet group (laboratory for Material Chemomechanics) at MIT has produced polydimethylsiloxane polymers with tunable viscoelastic moduli designed to simulate various internal tissues, resulting in PDMS samples that can be varied in stiffness from an order of 1kPa to 10MPa.[17] The material has also been used to replicate the viscoelastic responses of both heart and brain tissue.[17] PDMS is not only tuneable, but is non-toxic, non-flammable, transparent, capable of growing and hosting mammalian cells, and inexpensive.[1] A primary drawback of the material for the proposes of modelling is that as the stiffness decreases into the kPa range, the material becomes more and more adhesive; potentially confounding impact and indentation studies on the material.

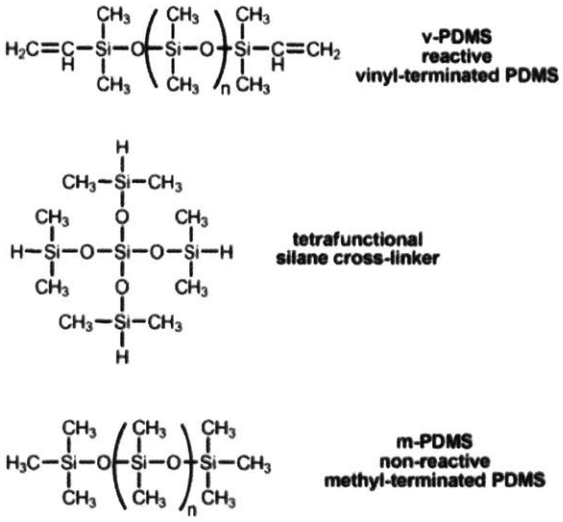

Figure 1-3. Structure of PDMS Gels: v-PDMS is reacted with various ratios of silane crosslinker resulting in m-PDMS whose viscoelastic properties are highly tuneable (from Mrozek et al.)[16]

In this thesis, both PDMS and gelatin are presented as case studies for finite element modelling for indentation and impact indentation respectively.

1.2 Mechanical Models of Compliant Materials

Organic tissues are some of the most difficult materials to fully characterize mechanically. They are often anisotropic, nonhomogeneous and nonlinear. Thissues can be self-healing, prone to either brittle or ductile failure, display adhesive qualities, be dependent or independent of temperature and pressure effects, and display poroelastic or nonlinear elastic behavior. Indeed, no real consensus of how to analytically describe many biological tissues exists.[18] Despite the complexity of the materials, many mechanical models of soft tissues and tissue simulants simplify the materials as frictionless, linear elastic or viscoelastic, isotropic, and incompressible. However, some work has been done to describe compression, failure and surface traction effects of the materials. In this thesis, elastic and viscoelastic properties form the basis for each model, but the effects of adhesion, shock loading and failure are also incorporated or investigated within the models.

1.2.1 Linear Isotropic Elastic Materials

The key characteristic of linear isotropic solids is that the material stiffness and compliance are independent of the direction of loading. That is, the material response depends only on two independent parameters (given by the Young's Elastic modulus E and Poisson ratio ν respectively) which can then be used to find both bulk modulus K and shear moduli G of the material. In most fields of engineering, characterizing materials as isotropic is an acceptable simplification of material constitutive models that can greatly reduce the complexity and computation time required to calculate or model materials response. Although tissues are not actually isotropic, it is still useful to assume this simplification to construct baseline models of

responses in many materials. In this thesis, most materials considered are idealized as elastic linear isotropic materials with modifications discussed below.

1.2.2 Viscoelastic Models

The strain of linearly elastic materials is only dependant on the stress applied to the material and its compressibility, and both shape and energy are recovered completely once an incident stress is removed. A viscous response, in contrast, links a strain rate to an applied stress, resulting in time dependent deformation and energy dissipation that is not recovered once the incident stress is removed. This irrecovered dissipation process is also referred to as hysteresis. Often, the elastic response is analytically characterized as a Hookean spring, while the viscous response is analytically characterized as a Newtonian dashpot. These analytical characterizations of elastic and viscous responses form the basis for modelling of various viscoelastic responses for tissues and simulants of interest.

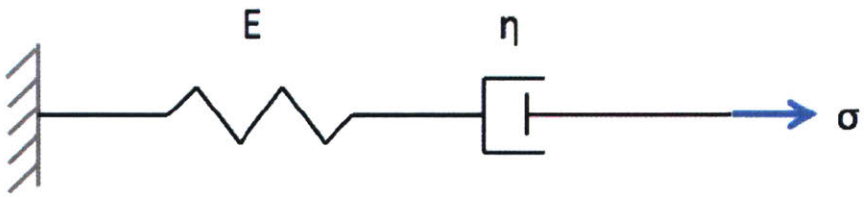

Figure 1-4. Maxwell Model of Viscoelastic Response: In the Maxwell model of viscoelastic response, the elastic and viscous components are placed in series. The elastic component is represented by a Hookean spring of stiffness E, and the viscous component is represented by viscosity η under and applied stress σ (From Demkowicz.[19])

One of the simplest viscoelastic models is the shown above in Figure 1.4, the Maxwell model of viscoelasticity. In this model, stress is constant across both elements, but total strain is based on the sum of the strains of each element. The elastic response contains a constant strain, but the viscous response contains time dependent strain resulting in material creep for as long as the stress is applied. Removing the stress results in elastic relaxation, but not viscous relaxation

resulting in permanent deformation of the material, which is not entirely consistent with the viscoelastic response of most tissues and simulants.

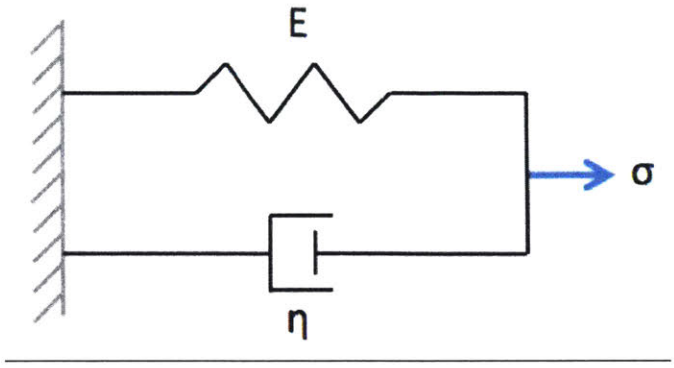

Figure 1-5. Voigt Model of Viscoelastic Response: In the Voigt model of viscoelastic response, the elastic and viscous components are placed in parallel. The elastic component is represented by a Hookean spring of stiffness k, and the viscous component is represented by viscosity η under and applied stress σ (From Demkowicz.)[19]

Another simple model of viscoelasticity is the shown above in figure 4, the Voigt Model. In this model, the applied stress is shared between elements, but strain is constant in both elements. Immediately on loading and unloading, the viscous component dominates, preventing instant response by the system. However, as the stress is applied over time, the strain asymptotically reaches a fixed magnitude constant given by the applied stress over the stiffness of the material. Removing the stress results in complete relaxation of the material back to its initial state. Though the response is different from the Maxwell model, this is also not entirely consistent with the viscoelastic response of most tissues and simulants. To create a model that better captures observed material responses, we turn to the Boltzmann superposition principle.

$$a_0\sigma + a_1\dot{\sigma} + a_2\ddot{\sigma} + \cdots = b_0\varepsilon + b_1\dot{\varepsilon} + b_2\ddot{\varepsilon} + \cdots \quad (1)$$

Based on the principle illustrated in Equation 1, an infinite number of appropriately scaled individual responses can be combined to approximately model the viscoelastic response of any

given material. In this way, the Generalized Maxwell Model (GMM), shown below in Figure 1.6, is analytically described.

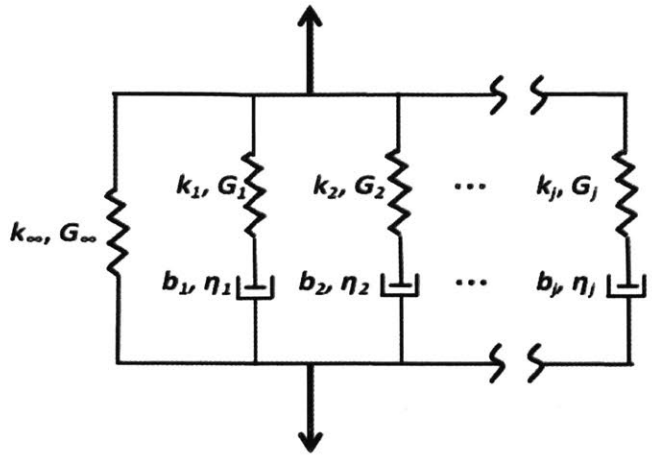

Figure 1-6. Generalized Maxwell Model: Also known as the Weichart model, the Generalized Maxwell model is the most general linear model to describe viscoelasticity. Like both the Maxwell and Voight models, the response of the Generalized Maxwell Model is a summation of pairs of Maxwell elements, defined by stiffness G_j and viscosity, η_j for materials yielding a relaxation time defined as $\tau_j = \eta_j / G_j$. Combined in parallel with another spring element, the Generalized Maxwell Model accounts for both creep and relaxation of materials. (from Mijailovic.[2])

In three dimensions, the constitutive model for a GMM is given by equation 2:

$$\sigma = \int_0^t 2G(t-\tau)\frac{de}{d\tau}d\tau + \mathrm{I}\int_0^t K(t-\tau)\frac{d\Delta}{d\tau}d\tau \qquad (2)$$

Where σ is the stress, e is the deviatoric strain, Δ is the volumetric strain and I is the identity tensor. $G(t)$ and $K(t)$ are the shear and bulk relaxation responses are given by equations 3 and 4 respectively:

$$G(t) = \mathrm{G}\infty[1 + \sum_{j=1}^{n} a_j^G \exp(-\frac{t}{\tau_j^G})] \qquad (3)$$

$$K(t) = \mathrm{K}\infty[1 + \sum_{j=1}^{n} a_j^K \exp(-\frac{t}{\tau_j^K})] \qquad (4)$$

Where $G\infty$ and $K\infty$ are the shear and bulk moduli as time tends to infinity, represented by the single spring in figure 3, and a_j^G and a_j^K are the residual moduli, given as a fraction of the instantaneous moduli coupled with relaxation times τ_j^G and τ_j^K representing the individual Maxwell elements, the number of which goes from 1 to n. The collective term for a given set of Maxwell elements is known as a Prony series.

In this manner, the stress response of the material depends on the timescale at which an impinging stress is applied, and allows for both creep and relaxation processes to occur. In this thesis, the materials under consideration are generally assumed to be isotropic in nature and generally incompressible, corresponding to a Poisson's ratio of approximately 0.5. Thus, volumetric relaxation is assumed to be negligible for all materials of interest and is not investigated within this thesis.

1.2.3 Hyperelastic Models

While linear elasticity is the simplest material to model, it often fails to describe materials responses at high strain states. In high deformation states, hyperelasticity, defined as a nonlinear isotropic elastic response governed by a strain energy function, can be used to model materials.[20] While the model can mimic tissue effects such as strain stiffening, the primary assumption that all deformation is elastic precludes the use of a viscoelastic material model. This thesis does not directly use or assume any materials are hyperelastic. However, the material constitutive models could be altered to include such a model in future work. Instead, for high strain deformation models, shock loading is considered.

1.2.4 The Effects of Shock Loading

The response of such materials to the rate of deformation is often of as much interest as the response to the given magnitude of deformation or applied load. As in the viscoelastic models discussed above, a load applied over a very long timescale can have markedly different

materials response to one applied quickly. Indeed, under a certain timescale (much quicker than the relaxation times of the Maxwell elements), the viscoelastic response itself becomes entirely negligible, and the material responds as a fully elastic solid. As one continues to decrease the timescale of loading, a new effect can be observed in nearly all ductile materials: shock.

Shock loading can be defined is a transient physical excitation derived from the sudden acceleration or impact of a load onto a material of interest.[21] A shock wave develops when a load is applied to a material at or near the speed of sound of the material, and results in compression of a material behind the shockwave. That shock front can alter material properties. Indeed, this compression can be heard in the sonic boom created when an airplane or a bullet pass the speed of sound of air, and is fundamentally of interest to many compliant materials including tissues and their simulants. One reason for this is that the low stiffness of such materials results in speeds of sound lower than the potential impact speed of many projectiles. Shock waves can cause a number of effects including elastic compression, permanent deformation, and phase transitions as shown on materials shown in figure 1.7.

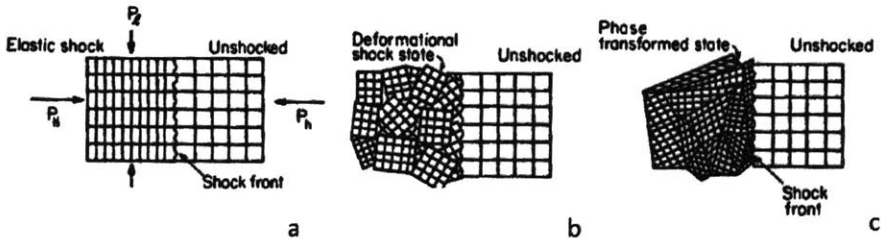

Figure 1-7. Effects of Shock: (a) The elastic shock occurs causing a highly-structured compression of material behind the shockwave. (b) The shockwave causes atomic lattice rearrangement of the material resulting in deformation of the material. (c) The shockwave causes a phase transformation of the material and growth of material along internal interfaces. (from Asay et al.[21])

While shock on tissues and their simulants may indeed induce a deformational or even potentially a phase transformed state, such models are significantly harder to analyse computationally (if they can be modelled at all). For the purpose of this thesis, all materials of

interest are assumed to behave as though they are elastically shocked. To analyse the effect of shock, we must establish an equation of state that relates the material properties in front of and behind the shockwave of interest captured in Figure 1.7 below:

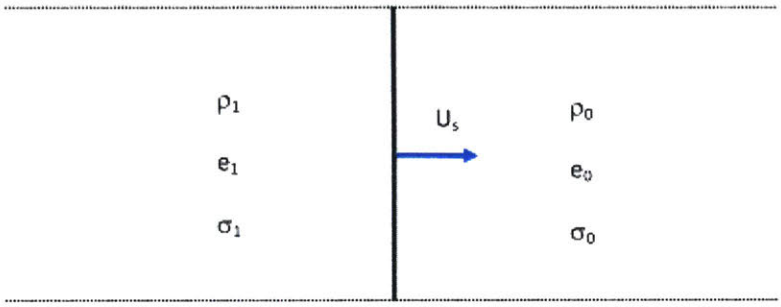

Figure 1-8. Shock Equation of State: This figure shows that the properties of density given by ρ, energy given by e and stress given by σ are relatable across a shock front of speed or velocity U_s (From ANSYS user handbook 2017.[22])

If we assume that density, energy and pressure can be varied across the shock front, and that mass, momentum and energy must be conserved across the boundary, we arrive at three conservation equations, collectively referred to as the Rankine-Hugoniot equations, given below:

$$\rho = \frac{\rho_o(U_s - u_o)}{U_s - u_1} \tag{5}$$

$$P_1 - P_o = \rho_o(u_1 - u_o)(U_s - u_o) \tag{6}$$

$$e_1 - e_o = \frac{(P_1 + P_o)\left(\frac{1}{\rho_o} - \frac{1}{\rho_1}\right)}{2} = \frac{1}{2}(u_1 - u_o)^2 \tag{7}$$

where ρ refers to the density, P refers to the pressure, e refers to the energy, u refers to the particle velocity, U refers to the shock velocity, and state 0 is un-shocked material while state 1 is shocked material.[22] To further simply the equations, it can generally be assumed that gauge pressure on the un-shocked state, P_o and particle velocity of the unshocked state u_o are equal to zero. In this simplest case of linear shock, knowing any three of the variables (usually U_s, u_1, and ρ_o being the easiest to measure) determines the shock state (assuming, of course, that the

shock speed or wavefront velocity is a constant in the material). Under these conditions, Equations 5, 6 and 7 simplify to Equations 8, 9 and 10.

$$\frac{\rho}{\rho_o} = \frac{(U_s)}{U_s - u_1} \tag{8}$$

$$P_1 = \rho_o u_1 U_s \tag{9}$$

$$e_1 = e_o + \frac{1}{2}u_1^2 \tag{10}$$

These equations give rise to the linear relationship common in many shock analyses:

$$U_s = C_o + s u_1 \tag{11}$$

Where C_o represents the bulk speed of sound of the material without the presence of shock (subject to the shear modulus of the unstressed material) and s represents the slope of the shock Hugoniot described in Figure 1.8.

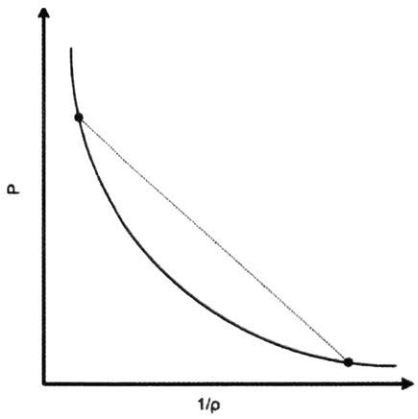

Figure 1-9. Shock Hugoniot: Pressure-volume plane of a material under load. If we consider the curve as what the material response would be if subject to non-shock loading, the straight line represents the material response at pressure during impact loading with a slope of s. (From Asay et al).[21]

At the high and low extremes of shock pressure, the shock loading does not affect the material, but during shock loading at any pressure between those points, the material response is governed not by the material curve but by the shock line, commonly referred to as a Rayleigh

line. The Rayleigh line is governed by rearrangement of the Rankine-Hugoniot equations given in Equation 12 below:

$$P_1 = U_s^2\rho_o - (U_s^2\rho_o^2)\rho_1 \tag{12}$$

The slope is given by $U_s^2\rho_o^2$ at the various states of shock denoted by ρ_1 and state 1 is any location along the Rayleigh line bounded by the Hugoniot curve.

Thus, shock can be described in linear materials via a shear modulus, which can be used to describe the bulk speed of sound of the material, and a linear fit relationship between the shock velocity and the particle velocity. However, the Rayleigh line and Hugoniot curve can be highly temperature dependent and requires one additional modification to complete the relationship between shock states: the Mei-Grunesien coefficient. The Mei-Grunesien Coefficient, $\acute{\Gamma}$, represents the thermal pressure of a set of vibrating atoms and is assumed to be independent of both pressure and energy states of the material and is described by Equation 13 below:

$$\acute{\Gamma} = \mathrm{V}(\frac{\mathrm{dP}}{\mathrm{de}})_V \tag{13}$$

which gives the following expression for pressure difference on integration:

$$P_1 - P_o = \frac{\acute{\Gamma}}{\mathrm{V}}(e_1 - e_o) \tag{14}$$

Equations 11 and 14 thus describe a material over the large range of temperatures and pressures commonly found in shock loading conditions. In this thesis, temperature is always assumed to be constant at room temperature (22° C), although the capability exists to alter the temperature profile of any model described herein. While shock plays a large role in the material response at high loads, material failure such as can also be responsible for observed materials responses within these extreme loading conditions.

1.2.5 Material Failure

In materials science, material failure is defined as the loss of load carrying capacity of a material unit, but different materials experience different failure methods and criterion. In brittle materials, failure is generally ascribed to the growth of cracks subject to a fracture toughness. This failure mode, called Griffith's brittle fracture theory, is governed by a critical stress or traction required to propagate a crack within the material described in equation 15 below:

$$\sigma = \sqrt{\frac{2Ey}{\pi a}} \tag{15}$$

where E is the Young's modulus of the material, y is the surface energy per unit area of the crack, and a is the crack length.[23]

For ductile materials, failure generally occurs after excessive strain deforms the surface of the material enough to exceed a given criterion. That may be as simple as exceeding a maximum shear stress as in Tresca yielding, or the strain energy density in von Mises yield criterion for elastic materials, or may be caused by a rate dependent inelastic behavior of the solid termed viscoplasticity, and governed by sliding frictional elements as shown in Figure 1.10.

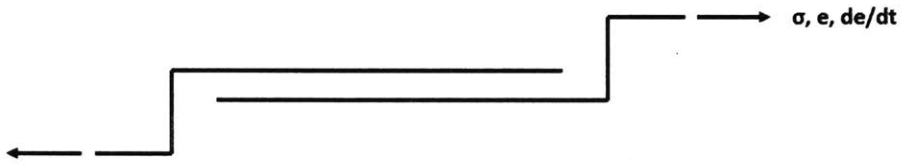

Figure 1-10. Sliding Frictional Element: This figure shows the concept of a sliding frictional element. The response of this element is governed by the applied stress, state of strain and strain rate on the material.

Unlike viscous and elastic response models discussed in section 1.2.2, a sliding frictional element only activates once a stress reaches a threshold yield stress.[24] At lower stresses, the element does not allow strain to occur, and results in permanent material change referred to as strain hardening after stress on the material exceeds that point. This type of deformation is plastic rather than the more commonly modelled elastic or viscoelastic deformation.

Various models detailing plastic deformation have been investigated including the Norton-Hoff model of perfectly viscoplastic solids and the Bingham-Norton model of elastic perfectly viscoplastic solids. In this thesis, materials modelled with ductile failure are assumed to deform elastoviscoplastically. That is, the stress within the material depends on both the plastic strain rate and the plastic strain magnitude.[25] This type of material has the benefit of being perfectly elastic or viscoelastic prior to exceeding the yield stress before adopting a plastic deformation mode. This results in a stress response detailed in Figure 1.11.

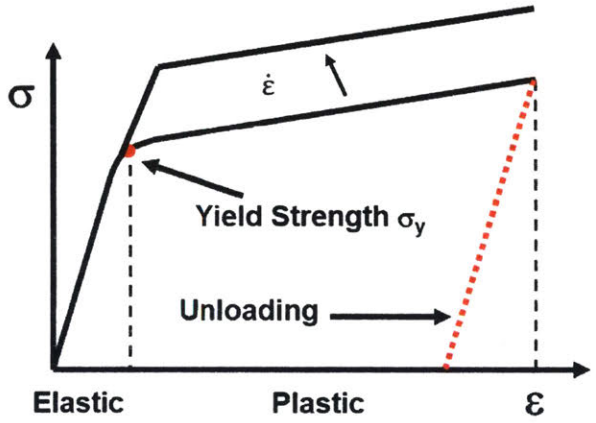

Figure 1-11. Elastoviscoplastic stress response: In this material constitutive model, stress is applied until a critical value of stress σ_y is reached. At this point, plastic deformation, also known as strain hardening, dependent on the strain rate, occurs until the final point of ductile fracture of the material (Adapted from ANSYS Mechanical Users Guide.[22])

In computational modelling at the continuum approximation assumed herein, allowing a material to fail at high stress states, is advantageous and desirable both to conserve the stability of the model and to accurately capture the material response at these extreme loading conditions. In this thesis, the Johnson and Cook failure model[26] is adopted to model failure at high strain rates, and is governed by Equation 16:

$$D = \sum \frac{\Delta \varepsilon}{\varepsilon f} \tag{16}$$

Where $\Delta\varepsilon$ represents incremental effective plastic strain and ε^frepresents the effective fracture strain of the material governed by pressure, strain rate and temperature dependence. ε^f is determined computationally by Equation 17.

$$\varepsilon^f = \left[D_1 + D_2\, e^{(D_3\sigma^*)}\right]\left[1 + D_4 \ln|\dot{\varepsilon}^*|\right]\left[1 + D_5 T^*\right] \quad (17)$$

In this equation, D_1, D_2, D_3, D_4, and D_5 are fitted unitless parameters, σ represents the stress, $\dot{\varepsilon}$ represents the strain rate, and T represents the temperature. If the sum of $\frac{\Delta\varepsilon}{\varepsilon^f}$ exceeds unity at any point during computational modelling, the element is said to have failed, deleting the element node instead of terminating the simulation.

While loads at high strain rates can be simulated using both shock and failure, at low strain rates, additional forces become relevant to the study of tissues and their simulants: surface effects. Surface effects are the complex interactions between molecules and atoms and can include anything from chain entanglements, covalent atomic bonding, ionic bonding, and even van der waals interactions between surfaces. Instead of investigating each type of interaction, this thesis concentrates primarily on the phenomena of adhesion between surfaces.

1.2.6 Effects of adhesion

Adhesion defined is the tendency of materials to stick to one another at adjacent interfaces. Computationally, adhesion is significant as it can confound indentation experiments or indicate erroneous mechanical properties. Clinically, adhesion is significant since changes in adhesion of tissues have been shown to be possible indicators of disease and may play a role in blunt force trauma. In mechanical terms, adhesion changes the contact area between two materials shown in Figure 1.12.

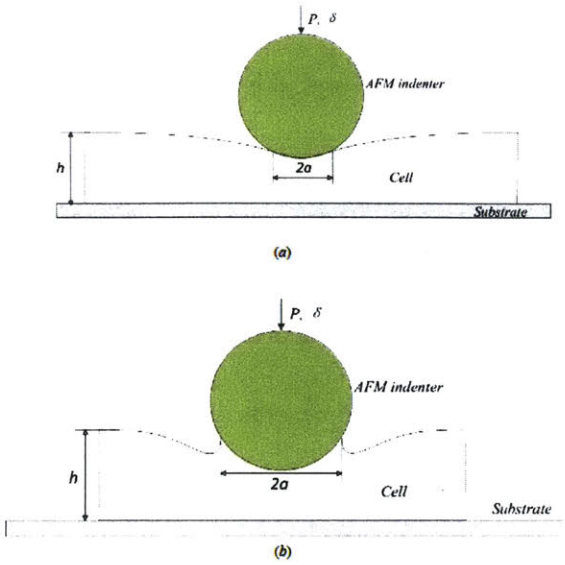

Figure 1-12. Perfectly elastic versus adhesive: Adhesion promotes a difference in contact between a rigid bead and an elastic layer with finite thickness. (a) Non-adhesive or Hertzian contact; (b) shows the contact with the application of adhesion. While the load represented by P and depth represented by δ remain constant in both models, the contact area represented by radius a increases with adhesion (From Zhu et al).[27]

In perfectly elastic contact, also called Hertzian contact, the radius of contact depends only on the depth of penetration and the radius of the indenter as shown below in equation 18:

$$a = \sqrt{Rd} \tag{18}$$

which is also given by:

$$a = \frac{3FR}{4E^*} \tag{19}$$

and results in a predictable maximum normal pressure P_o with load F:

$$P_o = \left(\frac{3F}{2\pi a^2}\right) \tag{20}$$

With a combined elastic moduli of the two materials expressed E^* as:

$$\frac{1}{E^*} = \frac{1}{E_1} + \frac{1}{E_2} \tag{21}$$

In adhesive contact a new term is included: γ the interfacial interaction energy between the materials which modifies the above equations according to a number of interpretations.

Adhesion can be modelled in several different ways, the first is a pure van der waals interaction given by the Leonard Jones potential. Another is the Derjaguin-Muller-Toporov or DMT model of elastic contact. Both models predict interactions between surfaces outside the contact area, but do not change the area of contact between indenter and surface. This is useful for stiff adhesive materials, but much less useful in extremely compliant materials such as tissues and simulants. In cases where the material is both compliant and highly adhesive, the Johnson-Kendall-Roberts or JKR model of adhesion is generally applied. In this model, the contact area is allowed to change based on the adhesive properties of both materials.

If we define work of adhesion as:

$$\Delta\gamma = \gamma_1 + \gamma_1 - \gamma_{12} \tag{22}$$

where γ_1 is the surface energy of the first surface and γ_2 is the surface energy of the second surface, and γ_{12} is the interaction term between the two surfaces, then we can say that the new contact area is defined as:

$$a^3 = \frac{3R}{4E^*}(F + 3\Delta\gamma\pi R + \sqrt{6\Delta\gamma\pi RF + (3\Delta\gamma\pi R)^2} \tag{23}$$

which collapses back to equation 20 if the work of adhesion is zero, and yields a maximum load of:

$$F_1 = F + 3\Delta\gamma\pi R + \sqrt{6\Delta\gamma\pi RF + (3\Delta\gamma\pi R)^2} \tag{24}$$

and a load at separation (commonly referred to as the pull-off force F_r) of

$$F_r = -\frac{3}{2}\Delta\gamma\pi R \tag{25}$$

1.3 Thesis Organization

In this thesis, we will explore two different timescales of loading as they pertain to soft tissue injury and design of tissue simulant gels.

Chapter 1 discussed the motivation, materials models and constitutive equations that govern the expected response of the materials in question.

Chapter 2 describes a finite element model of low velocity impact indentation and its modification to include adhesion as part of the investigation of surface effects. Comparison with experiments, and the limits of the model and its drawbacks are also discussed.

Chapter 3 describes two finite element model case studies of high velocity impact and their comparisons to other's available experimental data.

Chapter 4 presents the conclusions of this thesis and the directions for future work expanding and using the models presented herein.

2 INDENTATION MODELLING

2.1 Introduction

In this chapter, we explore a finite element model of indentation of polydimethylsiloxane, augment the viscoelastic model with the ability to sustain adhesive hysteresis, and analyse the effects of adhesive strength, strain rate and geometry on the material response.

2.1.1 Sample Preparation

In this thesis, PDMS samples used in experimental comparisons and in the materials properties used in modelling were created in the Van Vliet lab by myself and Bo Qing via the following procedure:

1) Polymer base and solvent (in this case CY-52-276A and CY-52-276B from Dow Corning) where weighed to a volume ratio of 4A:5B.
2) 15mL of sample were combined and mixed vigorously for 10 minutes.
3) The material was stored 2 hours under vacuum to prevent bubble formation.
4) The material was then poured into a Petri dish to a depth of 2 mm.
5) The material was then cured at 80°C on a level surface for another 24 hours.
6) After the material was cooled, a non-reactive surfactant was added to the surface of the material (to prevent adhesion during the removal process) and a die was used to cut and remove samples identical to the probe geometer of the rheometer (10 mm in diameter).
7) The underside of the material was then attached to sandpaper to prevent slipping during rheology (described in section 2.1.3 below) and the surfactant was cleaned off.

2.1.2 Viscoelastic Response investigation

Rheology is a branch of physics similar to fluid mechanics that deals with deformation and flow of solid matter under mechanical load over defined timescales.[28] There are numerous methods of conducting a rheological study on a given material, including cavitation[29] and indentation rheology,[30] however the most common method of obtaining flow data is through the use of shear rheology.

Shear rheology is a technique that fixes a flat, cylindrical sample of material in place, and applies a known torque T_o to the sample using a parallel plate which oscillates at a variable frequency ω, over an amplitude ψ which results in a deformation with strain of magnitude γ. Observing the difference between the applied deflection and the reactional torque allows a phase lag ϕ to be observed as shown in Figure 2.1.

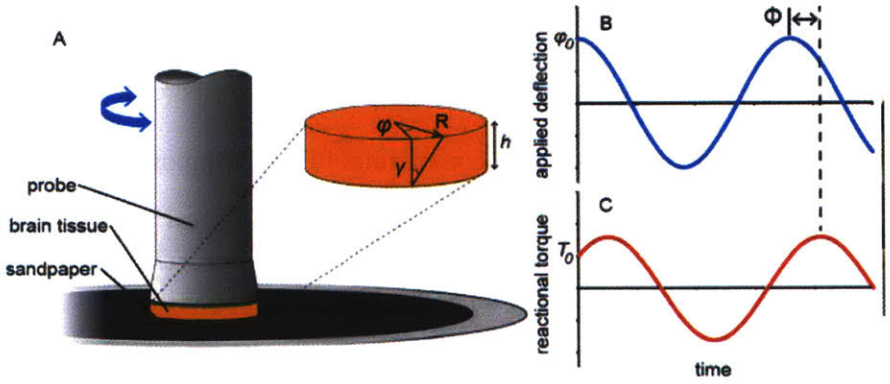

Figure 2-1. Shear rheology setup and phase lag determination: In figure A, the PDMS sample is fixed to the bottom plate of the rheometer using sandpaper to prevent slipping during testing. The top plate is lowered until contact is firmly established at 0.01N normal force, then is rotated at frequency ω and deflection amplitude ψ resulting in strain γ. In figure B, we see that the applied deflection is not perfectly synchronous (purely elastic) or asynchronous (purely viscous) between the reaction torque $\boldsymbol{T_o}$ shown in figure C indicating a viscoelastic response and necessitating conversion to the frequency domain to determine G(t). (From Canovic et al.)[31]

Varying the frequency of the rheometer establishes a time dependence of the material to load, and necessitates a conversion of the $G(t)$ given in Equation 3 to the frequency domain of both the storage and loss moduli of the material given in Equations 26 and 27, respectively.

$$G'(\mathrm{t}) = G_\infty + \sum_{j=1}^{n} \frac{G_j s^2 \tau_j^2}{1+s^2\tau_j^2} \tag{26}$$

$$G''(t) = \sum_{j=1}^{n} \frac{G_j s\tau_j}{1+s^2\tau_j^2} \quad (27)$$

Measurements are usually taken from shear strain oscillating frequencies of 0.001 to 100 Hz with inertial limits on the upper end, and signal to noise limitations on the lower end. Since shear strain at zero radius should be equal to zero, and maximum strain should be achieved at maximum radius, it is important to ensure that the sample being measured and the probe being measured have nearly the same (preferably identical) diameters. It is important to note that shear rheology is not designed to provide viscoelastic properties at shear strains beyond a few percent. The procedure for shear rheology is described in Canovic et al[31].

Summarized, parallel plate rheology was used by others in Van Vliet's group to measure *G*' and *G*'' at 25° C. Sandpaper was attached to the parallel plate to prevent slipping. A normal force was applied at 0.01 N to ensure continuous contact. Measurements were taken from 0.0159 to 15.9 Hz or 0.1 to 100 s^{-1} in angular frequency conducted at one percent strain, and from this plots of the storage and loss moduli for one commercial PDMS composition called CY52 and a stiffer PDMS coating (abbreviated SE) are presented in Figures 2.2 and 2.3. The Matlab code for generating the Prony series is contained in Appendix 1.

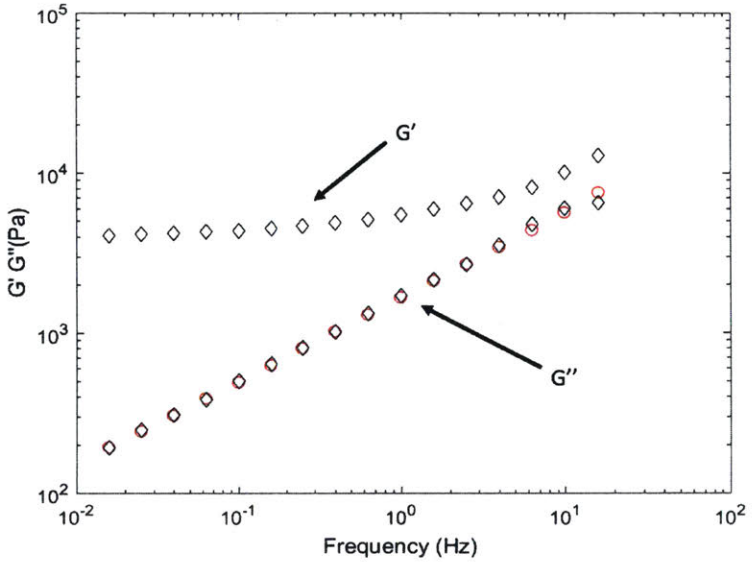

Figure 2-2. Rheology of CY52: Measured storage and loss moduli calculated between 0.0159 and 15.9 Hz. The storage modulus ranges from approximately 4 kPa to 13 kPa which represent the approximate G_∞ and G_o respectively while the loss modulus ranges from 200 Pa to 7.5 kPa. Both moduli contribute to the Prony series derived from fitting of these parameters. Data acquired by Bo Qing.

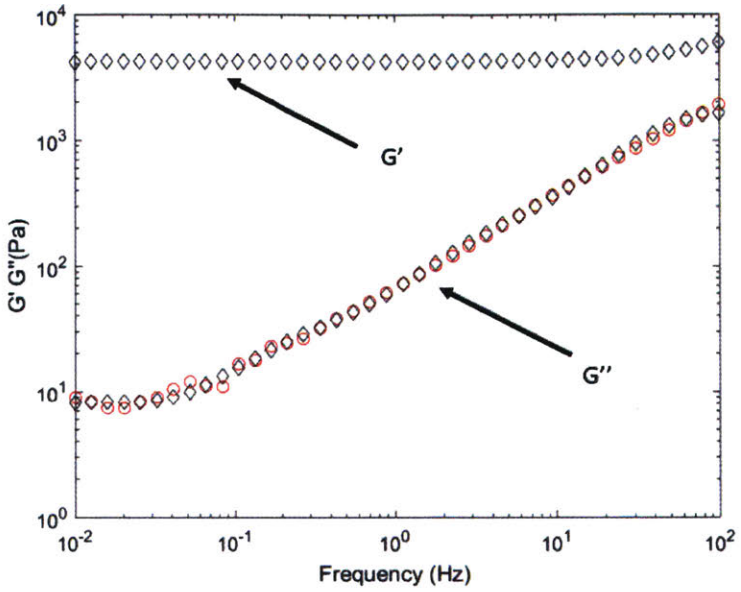

Figure 2-3. Rheology of Surface coating: Measured storage and loss moduli calculated between 0.0159 and 15.9 Hz. The storage modulus ranges from approximately 4 kPa to 9 kPa which represent the approximate G_∞ and G_o respectively while the loss modulus ranges from 10 Pa to 2 kPa. Both moduli contribute to the prony series derived from fitting of these parameters.

When fitting rheology data, a number of relative moduli and relaxation times corresponding to Equation 3 are determined. The number of Maxwell elements fit can be anywhere from one element to over one hundred elements which are termed a Prony Series. Too few elements can result in a misrepresentation of viscoelastic materials response, while too many can result in overfitting that only serves to increase computational time and effort for increasingly marginal increases in accuracy.[32] For this thesis, four Maxwell elements for CY52 were calculated and the fitting of the four relative moduli and relaxation times yields a prony series given in Table 2.1, for data acquired by Bo Qing at a temperature of 22°C. Relative moduli are fractions of the instantaneous modulus of the material and can be converted into to units of Pa via multiplying the relative moduli fraction with the instantaneous modulus G_o. This means at

any given time there is a remainder shear stiffness located between the infinite (time tending to infinity) and instantaneous modulus of the material (time tending to zero).

Table 2.1: Relative moduli and respective relaxation times of Commercial PDMS (CY52)

Index	Relative Moduli	Maxwell Modulus (Pa)	Relaxation Time (s)
1	0.6646	9237.94	0.0629
2	0.0868	1206.52	0.7866
3	0.0286	397.54	5.6475
4	0.0123	170.97	42.455

2.1.3 Experimental Setup

Figure 2.4 shows the schematic of the experimental apparatus used in analysis of adhesive gels within the Van Vliet Group. The pendulum is fixed to a supporting frame and allowed to pivot freely into and away from the sample. Both a flat punch and a spherical geometry can be used to indent samples, but a spherical indenter provides much better information about surface effects described in chapter 1. The sample itself is mounted on a post and positioned at a distance such that the indentation occurs with nearly all displacement directed into the longitudinal axis of the sample. Through use on an electromagnetic coil, a load is applied to the top of the pendulum. A parallel plate capacitor, mounted on the same axis as the indenter is used to measure the displacement of the pendulum during indentation. At the base of the pendulum, magnetically soft iron is attached so that a solenoid can be used to retract the indenter. The entire setup is enclosed and temperature controlled to prevent undue influence from ambient interference.

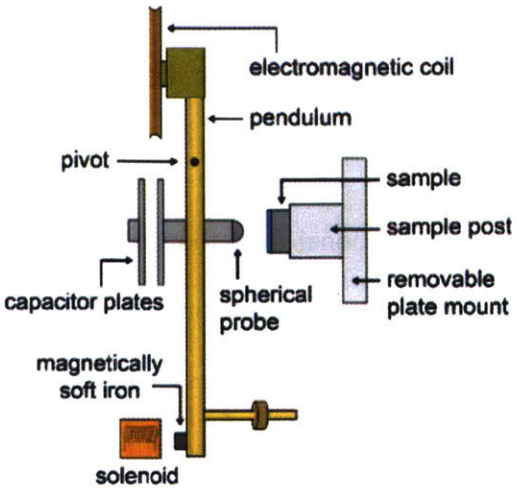

Figure 2-4. Experimental Setup: Experimental data was acquired by Bo Qing using this pendulum indenter setup (From Qing et al.[33])

During an experiment, the current is fed through the solenoid to draw the indenter away from the sample. The sample plate is then moved in the direction of the indenter at a distance of 0.5mm to ensure axial indentation of the sample. Then a current (of amplitude that determines the force of impact) is applied to the electromagnetic coil and is maintained throughout the test. (This represents a force controlled experimentation profile.) Once the solenoid is turned off, the pendulum is free to impact the indenter, and the response is recorded via the capacitor plate mounted behind the indenter. Zero displacement should correspond to the point of contact at the material surface. This experiment can be modified to include a liquid cell attached to the sample post. This is primarily used for keeping samples hydrated and reducing surface effects via the use of surfactants. This thesis, does not include data acquired using the liquid cell.

2.2 Finite Element Modelling

Finite Element Modelling is a numerical method for solving problems in engineering and physics. The technique discretizes structures into small element sets governed by constitutive laws like those discussed in chapter one. These elements have a finite number of degrees of freedom, or nodes that allow the finite element model to respond to impinging stress, strains or

pressures. The discretized nature allows for investigation of specific phenomena such as local stress concentrations or surface effects that may not be applicable to the bulk structure.[34]

2.2.1 Representative Volume Elements

The concept of scaled computational modelling is fundamental to the accuracy of the models in question. While an infinitely sized and infinitely refined model of a body would undoubtedly provide the most accurate material response, this approach is computationally impractical if not impossible and provides marginal benefits past a point of model convergence. On the other hand, a model sized too small will fail to provide accurate material responses to imposed loads especially if the material is heterogeneous in nature or contains inclusion bodies such as fibres or particles that may locally alter response of the material, or if the size of the model allows the effects of the bounded edges to become integral to the materials response.[35] In this model of PDMS, the crosslinked network would be matrix material, while the solvent would be the inclusion. To reconcile the wants for both computational speed and accuracy, the concept of a Representative Volume Element (RVE) is used.

An RVE is defined as an element whose length scale is infinite relative to the microscale local interactions of any singe heterogeneity.[36] In finite element modelling (FEM), this translates to having elements large enough such that no given inclusion would play an undo effect on the response of the bulk material. However, the smaller the element size the more accurate the material model should be, which leads to the concept of multiscale or multizone materials model meshing shown in Figure 2.5.

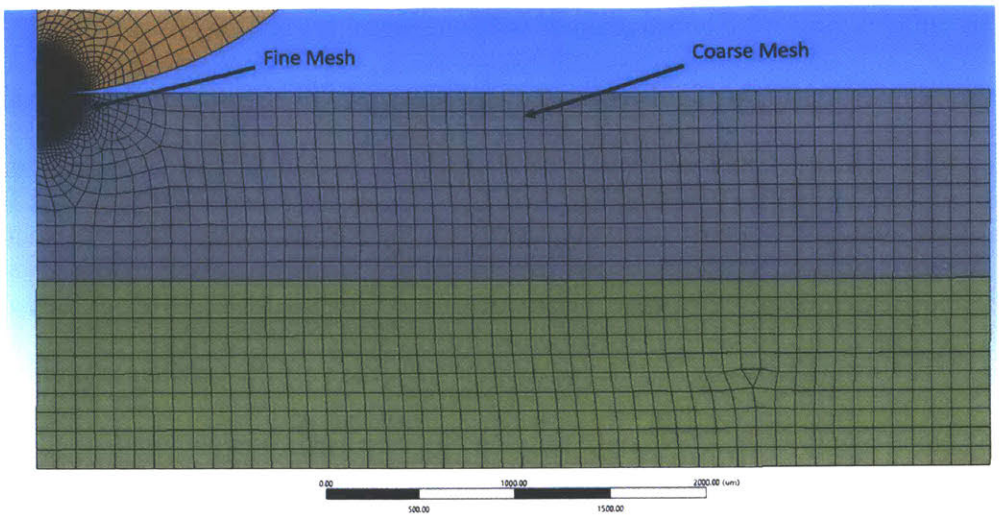

Figure 2-5. RVE Mesh and Sizing: Multizone meshing was implemented in the model based on contact location. Specifically, we used vertex sphere of influence sizing for both the indenter and the half plane, resulting in a highly-refined mesh within in the contact area. This was designed to provide great resolution in the area of contact while the coarser mesh on the far away from the contact area provides macroscale resolution without sacrificing either computational time or accuracy.

Since we estimate that inclusion pockets of solvent would be on the order of nanometers in size,[37] it would be reasonable to assume that minimum finite element size for the model would have to be one micrometer or greater to approximate a continuum representation. In this model, the smallest mesh element is seven microns in length on all sides while the largest is 100 μm in width and height.

2.2.2 The Finite Element Model

The model was developed using the commercially available ANSYS finite element modelling software version 17.2, using a license available from DRAPER laboratories. However, the models contained herein can mostly be completed using the universally available ANSYS student version. Key features of the licensed version needed for this thesis work not available in the student version are the lack of restriction on node count and density enabling case studies at high resolution, and the high performance computing (HPC) feature that enables multicore and GPU acceleration of the model allowing simulations to be completed much faster.

The samples used were constructed of two, one mm thick sections of gel, bound together into one two mm thick sample of gel. These sections have a width of five mm. These sections are tunable in both thickness and material type for use in testing bilayer constructions while maintaining geometric symmetry with samples tested in the rheometer and the experimental setup. The model was designed to take advantage of the computational power of axisymmetric modelling. 3D elements can provide finer resolution for certain effects (such as material failure), but for this model, they would only apply significantly increased computational simulation time without providing additional accuracy or understanding. The model is detailed in Figure 2.6.

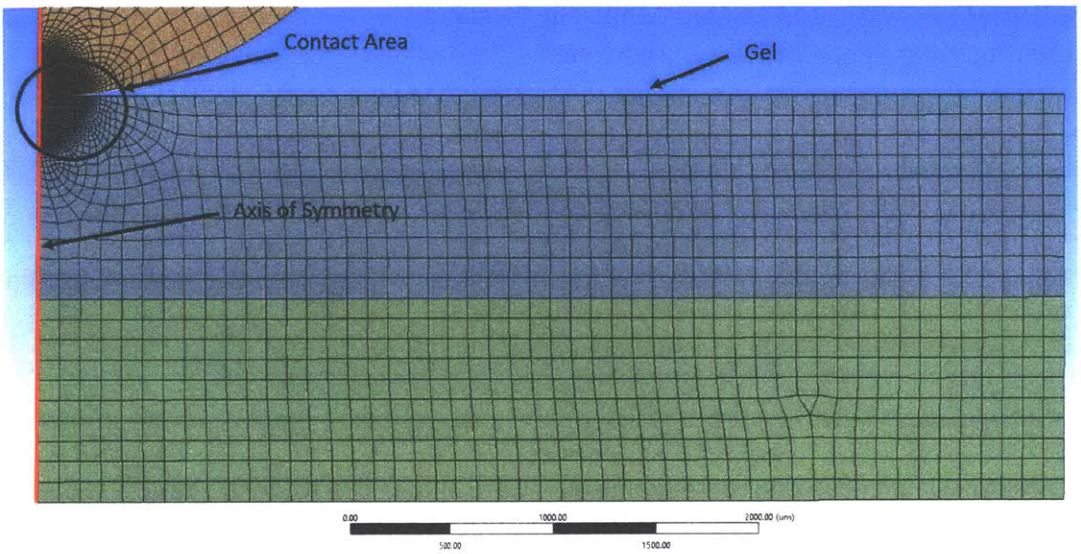

Figure 2-6. Model Setup: The axisymmetric mesh was constructed via multizone method allowing the mesh coarseness to increase the greater the distance from the contact point. The base of the gel is bounded by a fixed support to prevent movement of the gel during the indentation process. It is important to note, that the fine mesh of the contact area must include the entire contact area to be observed during contact as surface effects will propagate from the edges of contact through the rest of the contact area. Scale bar is included.

One key initial step in establishing a finite element model is via performing a mesh convergence study.[38] This is accomplished by controlling for one variable (usually whatever is deemed most important for the study) and then systematically increasing the density of the mesh. If a mesh is too coarse, it may still run the simulation to completion, but then as the mesh is refined, the controlled variable output will change in value. A mesh is selected for use in the

simulation when further refining of the mesh (decreasing of element dimensions and increasing number of elements) presents no significant change in the value of the controlled variable. This represents the point at which the additional computation time is required for increasingly low increases in model accuracy. To validate the adhesion model setup, the pull off force was selected to be the controlled variable, and the mesh was systematically varied from 4000 elements to 28,000 elements.

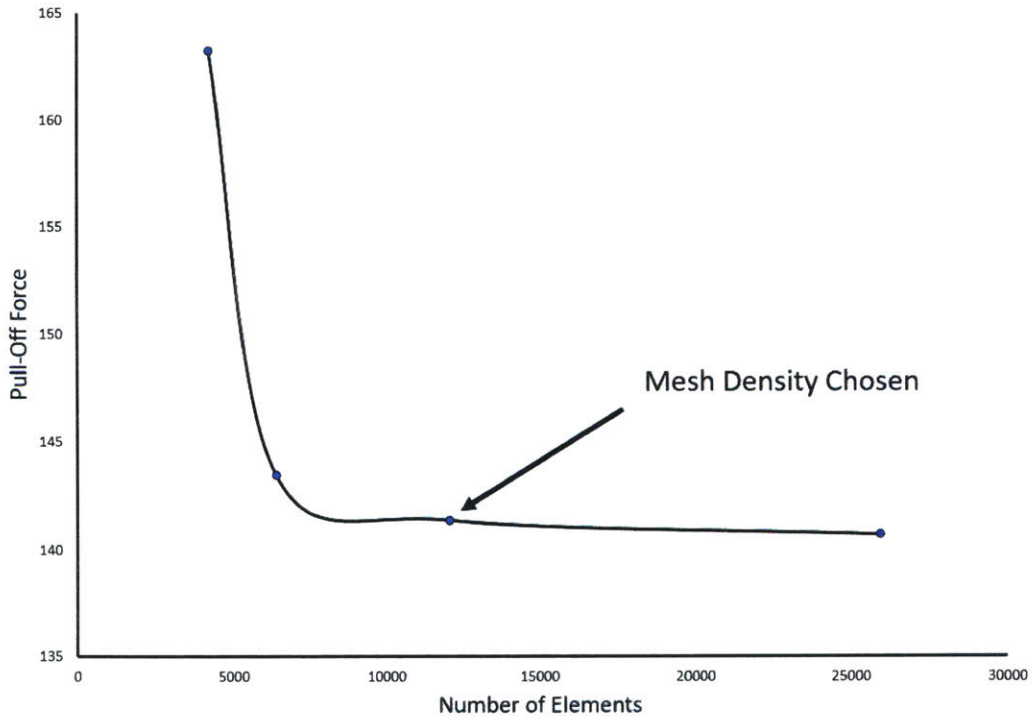

Figure 2-7. Mesh Convergence Study: In this convergence study, the pull off force of determined during the adhesive trials discussed in section 2.3 was evaluated as the most important indicator of the study. For accuracy, the number of elements selected was 12,000. An increased mesh density would undoubtedly be more accurate, but the degree of increased accuracy was determined to not offset the added computational cost.

The spherical indenter was modelled using structural steel. While the indenter should not undergo any real deformation during the indentation process (as it is several orders of magnitude stiffer than the gel in the model), it is modelled as a deformable solid to ensure that any surface interactions were modelled as accurately as possible.

This experiment was conducted via displacement controlled indentation. The spherical indenter was indented into the material at a rate of two microns per second (which is consistent with the experimental setup and procedure) for forty seconds resulting in a total displacement of eighty microns. The indenter was then fixed at eighty-micron depth for forty-eight seconds to allow for relaxation of the material. The indenter was then lifted from the material at a rate of two μm/s per second, past the zero point, and up to 74 μm above the surface. The full plot of the displacement profile is given in Figure 2.8:

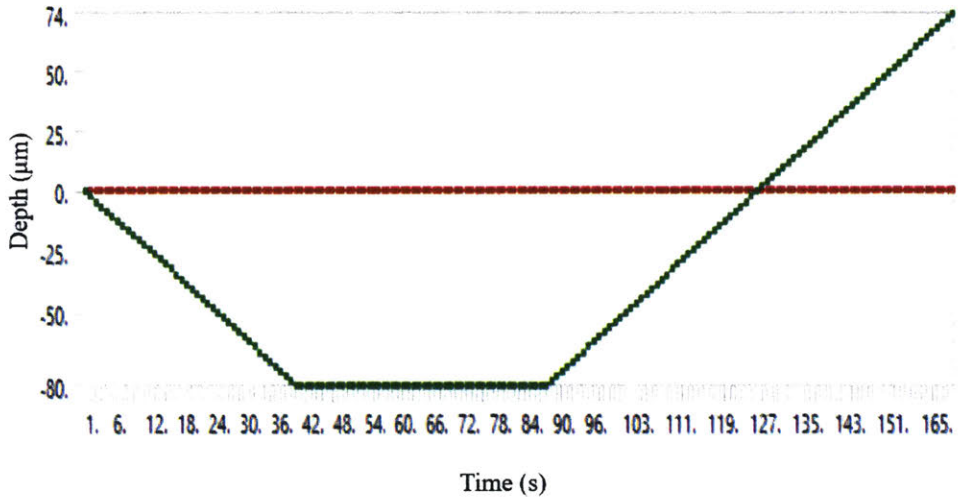

Figure 2-8. Displacement Controlled Profile: Here we show the displacement control of each step. The green line represents the y-axis, the axial direction of loading. Note the loading and unloading occur at two microns per second, and the indenter is allowed to move past the zero-displacement point. The red line indicates constrained movement in the lateral or x direction.

2.2.3 Viscoelastic Results

In the simplest use of the model, the case of viscoelastic response was investigated. Surface effects such as adhesion were not implemented. Using the Prony series derived from the fitting of rheological data described in section 2.1.2, the model results were compared to results obtained with the spherical indenter described in section 2.1.3 and are shown in Figure 2.9.

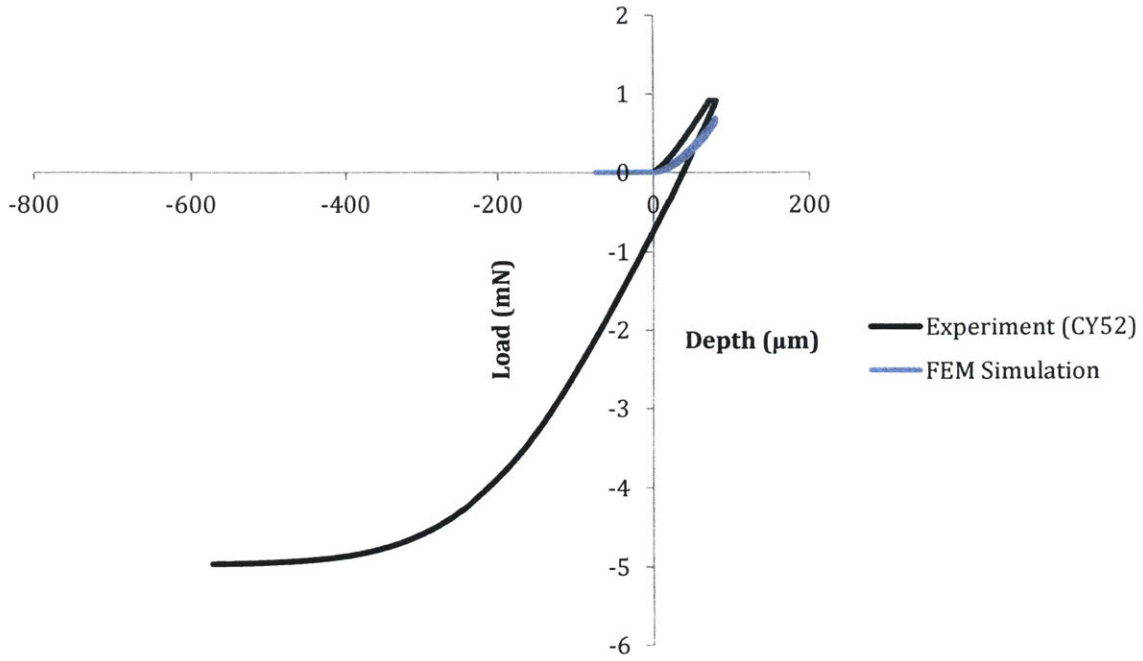

Figure 2-9. Indentation Experiment and Model comparison: In this figure, we show that experimental data on the commercial PDMS sample called CY52 and the FEM model output. Note that the model does not include adhesion.

While probe and gel are geometrically identical (with probe radius of 2 mm and gel thickness of 2 mm and radius of 5 mm), and final depth of penetration was similar, there are obvious differences in response that can likely be explained by a few factors. First, the experiments operated in load control, simulations were conducted in displacement control. In theory, this difference in constant loading rate or constant displacement rate should not greatly effect affect the maximum load or dissipation energy at equilibrium in quasi-static deformation case, so this is a minor reason. Second, the rate of loading is significantly lower in the FEM simulation than in the experiment on the CY52 PDMS. One would expect a higher loading rate to produce a stiffer response (sharper loading curvature, and lower depth at a given maximum load). As we see later in figure 2.18, the assumption that loading rate positively corresponds to maximum load is substantiated. Additionally, this iteration of the FEM did not account for adhesion, which certainly played a significant role in the experiment as evidenced by pull-off

force. Ultimately, the difference in depth of penetration, between the model and experiment was less than an order of magnitude. For the purposes of this thesis in which we want to investigate the role of adhesion and viscoelastic properties, and not merely replicate experimental results, the simulation sufficiently approximates experiments that it can be used for parametric studies.

2.2.4 Implementing Adhesion

Adhesion is not a implemented readily in ANSYS software, and cannot be directly implemented as an input parameter such as surface energy. However, the software is built on a Fortran core functionality and is inherently modifiable with the right console commands input at the correct times during a simulation.[39] To explain how this is done, first note the workbench file architecture in Figure 2.10.

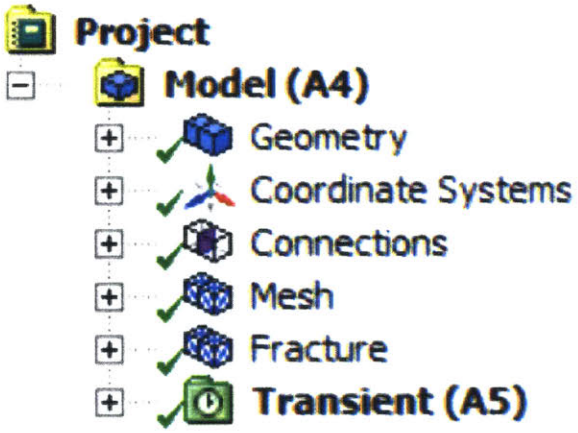

Figure 2-10. Workbench File Architecture: This is the project architecture in ANSYS workbench.

As shown in Figure 2.10, there are six distinct sections imposed in these models. The first is geometry, in which materials assignments are implemented. The second is coordinate systems that provide a unified, bounded box of component (or "part") interactions. The third is connections among components and in this bock contact type is established between components and potentially modified. The fourth is mesh, where components can be systematically and specifically meshed to provide the greatest accuracy. The fifth is fracture. This section is

implemented in these experiments but it is not standard in most workbench applications. The last is the transient section, this is the control system of a workbench project. Here, the analysis settings, conditions, loads, displacements are initiated and command modifications may be input at any simulation step desired.

To implement adhesion requires first assigning a de-bonding condition. To do this, we implemented a fracture energy based de-bonding method used for cohesive zone modelling. This method uses the concept of brittle elastic fracture discussed in chapter one. It assumes that the surfaces in contact separate based on the propagation of a crack between the surfaces that separate under Mode I or tensile fracture at the interface between the materials. Two terms are required to accomplish this, a maximum normal contact stress and a fracture energy. The relationship between the two is given in Figure 2.11.

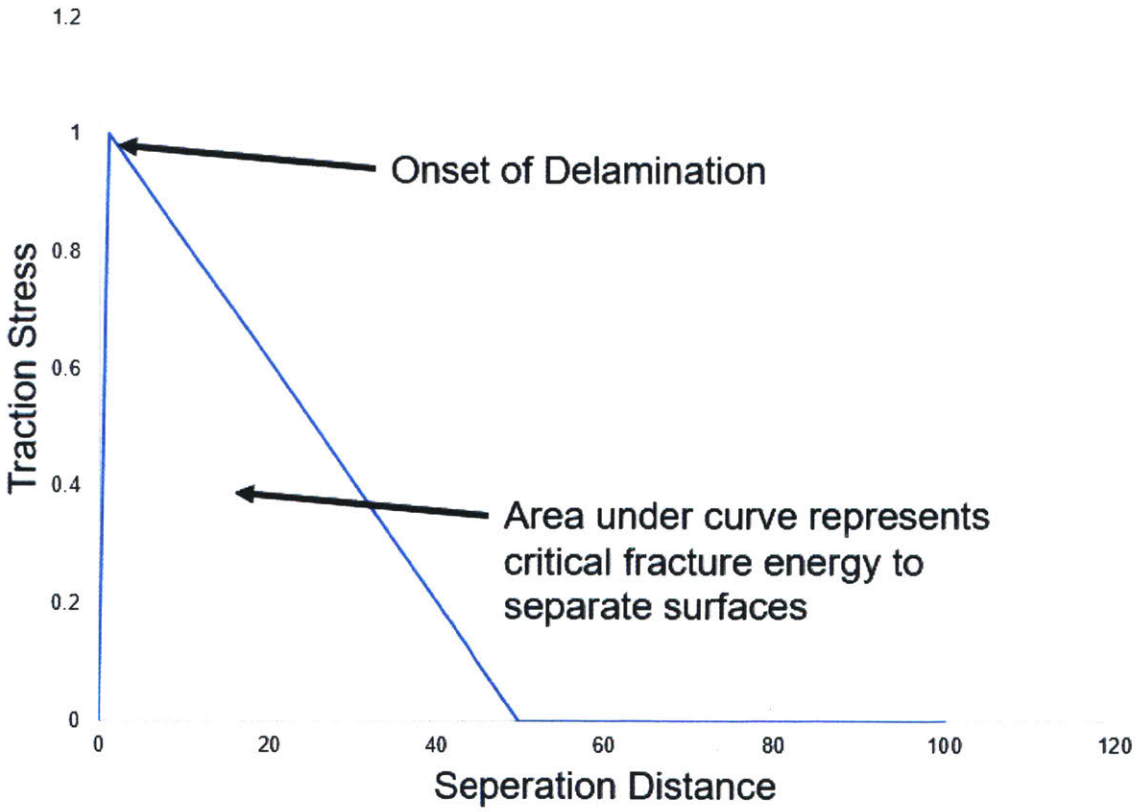

Figure 2-11. Fracture Energies Based De-bonding: This figure shows the interaction between critical stress and fracture energy. Until the maximum stress is reached, no de-bonding occurs. Once the de-bonding occurs, the energy required to fully separate the nodes is given by the input fracture energy. While both parameters play a role, separation cannot occur until the critical traction stress is reached, and thus this is the parameter primarily optimized.

After selecting values for both critical traction stress and fracture energy, we then implemented de-bonding. First, we set the ANSYS "contact body" to the more compliant of the two bodies (i.e. the polymer) and the target body to the stiffer of the two bodies (i.e. the indenter). Though you can assign the stiffer body as the contact body, the penetration prevention algorithm (refered to as the Augmented Lagrange algorithm) requires the more compliant body to be the contact body in a given pair if you wish to prevent surfaces from moving though one another. Additionally, a cohesive zone model cannot be implemented unless the more compliant body is assigned as the contact body which would prevent the implementation of adhesion. Next, we set the contact status between the contact and target to "bonded," computed by the Augmented LaGrange algorithm for use with compliant materials. For a spherical indenter, implementing bonded contact at step 0, or initialization, would normally cause irreconcilable mesh distortions upon running the simulation. This is because the surfaces would attempt to immediately deform and adhere to one another. Instead we modified the contact upon initialization of the model using a command override shown in Figure 2.12.

Figure 2-12. Modification of Contact: Bonded contact is applied between the surfaces but modified at step zero. Override commands are given by creating an insert called Commands ADPL. ADPL refers to the underlying mechanical code that ANSYS runs on. Modifying this code modifies can modify the core functionality of an ANSYS sim, and in this case, facilitate the implementation of adhesion.

To modify the initial contact status, we use an unlisted keyopt modification command, keymod, to change the bonded status keypoint. The precise code is:

Keymod, cid, 12, 0

This code tells ANSYS that we are changing a keypoint variable, on the cid or contact body (which is reciprocated on the target body), specifies that we are changing the contact surface interaction (denoted by variable 12) to frictionless denoted by the final variable 0. Thus, the contact is defined as bonded, which allows us to assign the fracture mechanic to the surface, but avoids the mesh instability caused by the initial distance from contact to target surface. This modification treats the contact as frictionless until we modify the contact at a later point in the simulation illustrated in Figure 2.13.

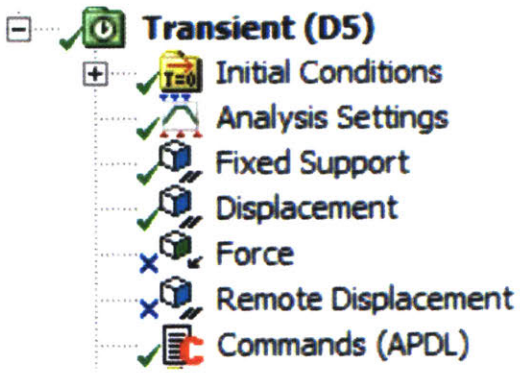

Figure 2-13. Transient Control System: The control section of ANSYS workbook allows for stepwise modification of key parameters. For our purposes, we modified the bonding condition during the relaxation time of the simulation using another Commands (ADPL) insert.

Using another command prompt delivered during a relaxation step (a timestep denoted by the line of zero slope in figure 2.8, where the change in contact area is negligible, we can restore the bonding state. To do this we used the unlisted keymod command:

Keymod, cid, 12, 3

Much like the first code, this phrase resets the contact parameter from frictionless to bonding without the detriment of distorting the mesh to achieve contact. This allows the model to run to completion and ensures that adhesion is both a tunable and a explorable surface phenomena in

this thesis. An example comparison between the non-adhesive viscoelastic response and an adhesive viscoelastic response is detailed in Figure 2.14.

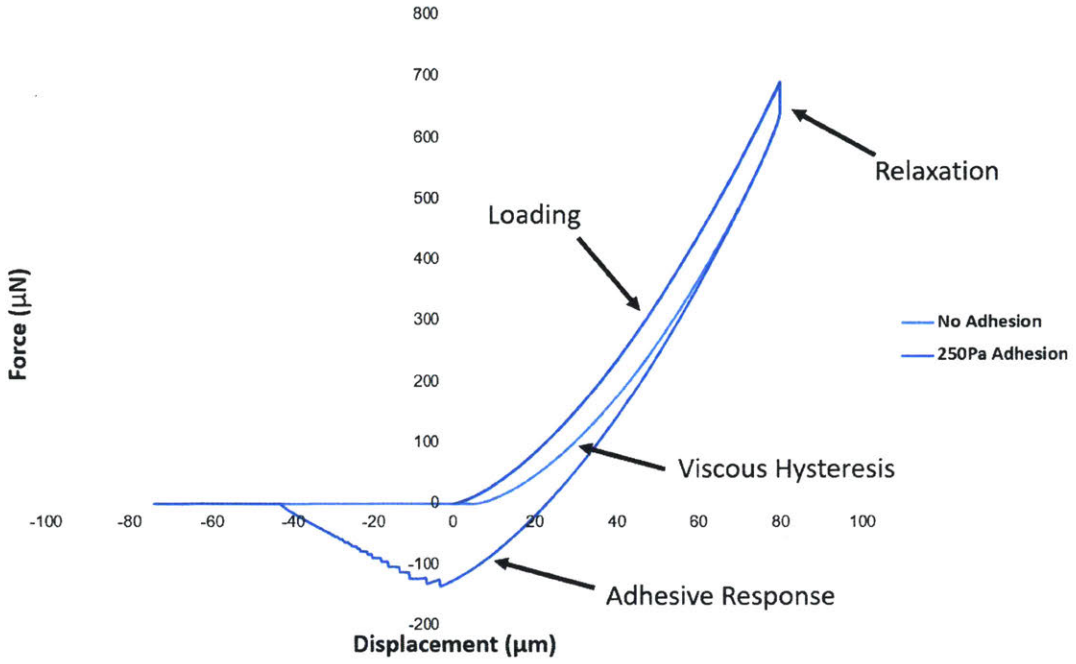

Figure 2-14. Non-Adhesive versus Adhesive Response: Here we detail the difference between adhesive and non-adhesive response. Loading profiles are the same, since adhesion is not applied until maximum contact area is reached during the relaxation phase. While both models contain some viscous hysteresis, the adhesive response is characterized by a diverging contact profile as the contact area does not decrease at the same rate as the frictionless contact of the non-adhesive response.

2.3 Investigating Adhesion

With the above model, we next explored explore several questions related to its application, including the effect of adhesion, the effect of strain rate on adhesive response, and the quantification of energy dissipation, or hysteresis, caused by adhesion. For the following experiments (unless otherwise specifically noted), the polymer is assumed to behave as a viscoelastic material, whose Prony series was defined in table 2.1 and the indenter is assumed to be structural steel, with an elastic modulus of 70 GPa.

2.3.1 The strength of adhesion

To test how the response of the model was affected by the magnitude of adhesion, we selected values for the critical stress component along several orders of magnitude for testing ranging from 25 Pa to 25000 Pa. Importantly, we did not vary γ_{12} directly, but this relates to the critical traction stress. Stress delamination, described in Figure 2.11, could be related to a calculated interfacial energy indicative of relative "adhesion strength." For this range of traction stresses, our approximate γ_{12} ranges from 0 to 80 mJ/m^2 (see Figure 2.23). We acquired load-displacement profiles shown in Figure 2.15. Note that the output files record reaction "reaction force" and probe "displacement."

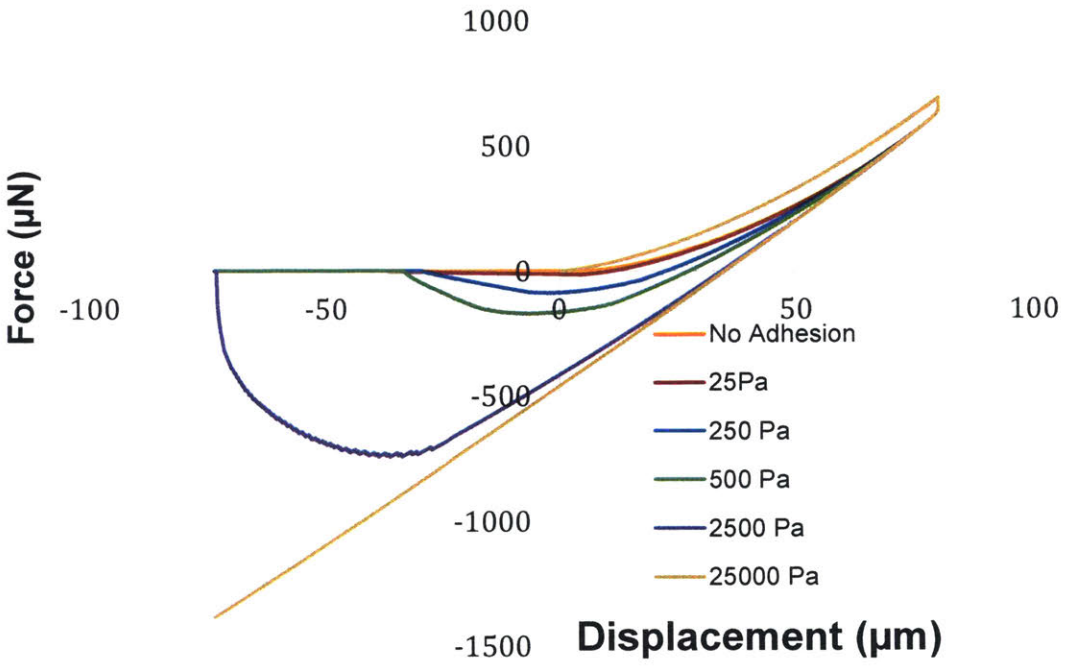

Figure 2-15. Effect of Adhesive Strength: Effect of increasing critical traction stress (related to adhesive strength) on the material response.

As the strength of adhesion increases, the profile of the response approaches a linear unloading condition. Highly adhesive conditions demonstrate less change in indenter probe-polymer contact area during unloading, as compared with less adhesive polymer models (lower traction stress prescribed). At the most adhesive conditions, change in contact area is essentially

negligible throughout the unloading process throughout the displacement analyzed. We refer to conditions with negligible change in area as fully adhered states.

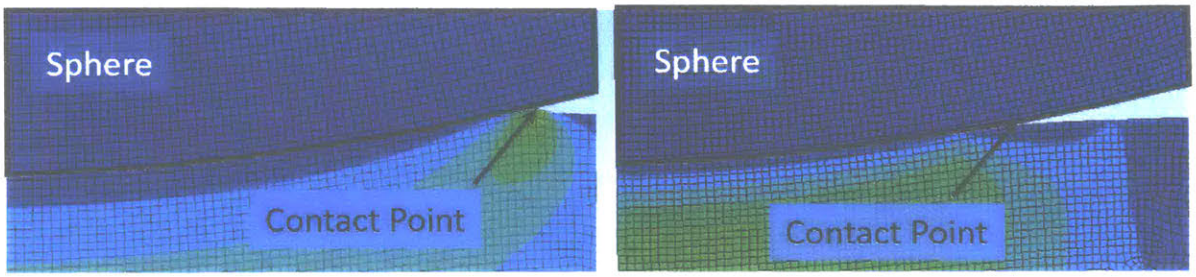

Figure 2-16. Contact Area Comparison: This comparison between model trials at 2500Pa (left) and 250Pa (right) at load step 110 (about halfway through unloading). The contact area is reduced resulting in a change in loading profile. As critical pressure increases, the reduction in contact is reduced until the point at which there is no quantifiable change in contact area over the unloading timescale.

This fully adhered state, in which contact area is not changing during unloading, behaves much like an indenter of different probe geometry: a flat punch. The comparison between a flat punch indenter of radius equal to the radius of the contact area of 2 mm spherical indenter at maximum displacement (450 μm radius at 80 μm in depth) is shown below in figure 2.17.

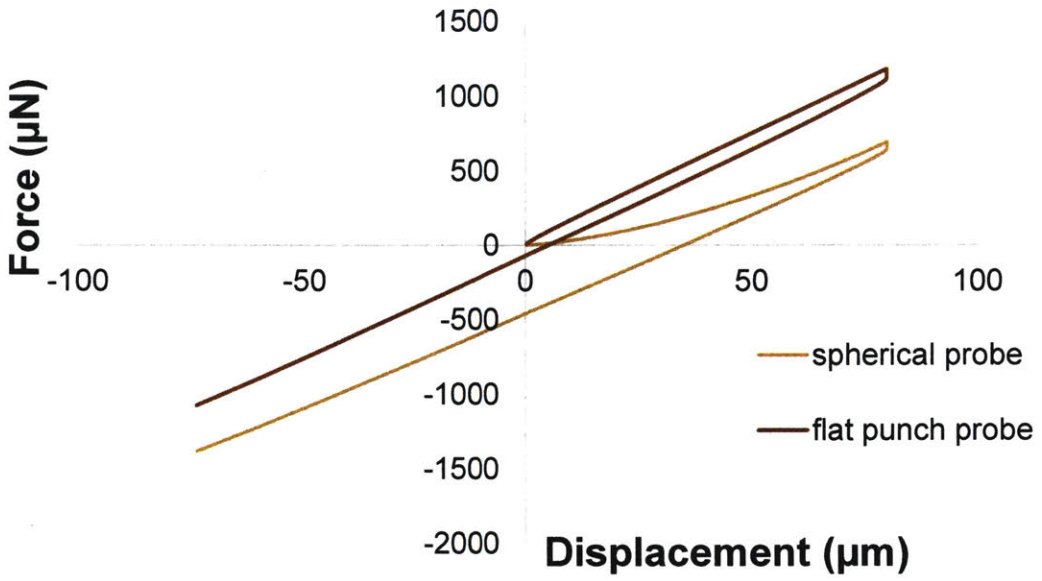

Figure 2-17. Comparison between Flat Punch and Spherical Indenter: FEM output similarities in the unloading profile between a fully bound sphere and a fully bound flat punch indenter. While the final loading and unloading forces are different, the unloading profiles are very nearly similar and linear. Since there is no change in area in the fully adhered case, this makes sense. For both probe geometries, the traction stress was 25000 Pa.

2.3.2 The effect of probe displacement rate on Adhesive response

While neither Johnson-Kendall-Roberts (JKR) adhesion or elastic fracture models detailed in chapter one predict or address the rate of strain on the adhesive response, it is nonetheless an interesting question to explore with the finite element model. Strain rate dependence on linear viscoelastic materials has been shown to increase with increasing strain rate.[40] To simulate this, the rate of probe displacement was varied from 1 μm/s to 16 μm/s, while the maximum indentation depth was held constant. The simulation paused for 10 seconds at maximum depth to allow for relaxation regardless of the loading and unloading rate to ensure we compared the unloading differences from an approximately equivalent starting condition. The results are contained in Figure 2.18.

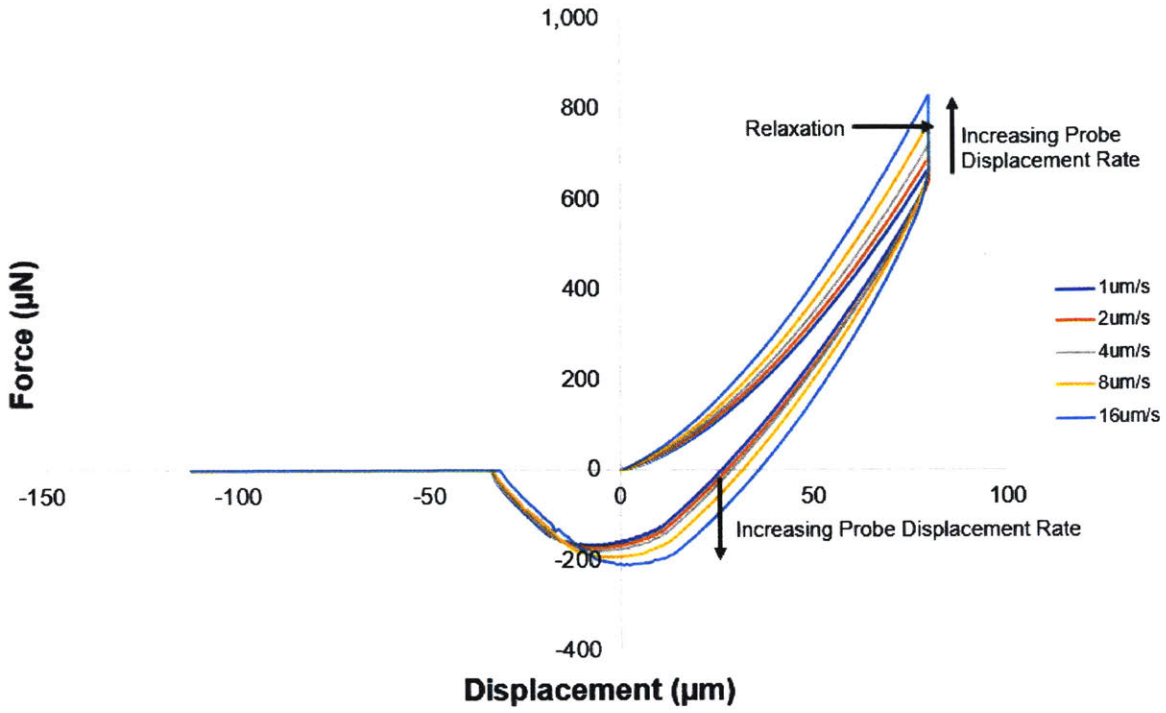

Figure 2-18. Effect of Probe Displacement Rate on Reaction Force: Increasing probe displacement rate in both loading and unloading affects load-depth response of model viscoelastic polymer. There are two clear trends, an increase in maximum reaction force and an increase in pull off force.

This figure illustrates two independent phenomena. First, increasing the probe displacement rate of loading increased the maximum force at the same final depth of indentation. Second, increasing the unloading rate increased the maximum pull-off force experienced by the material. This is shown in figure 2.19 below:

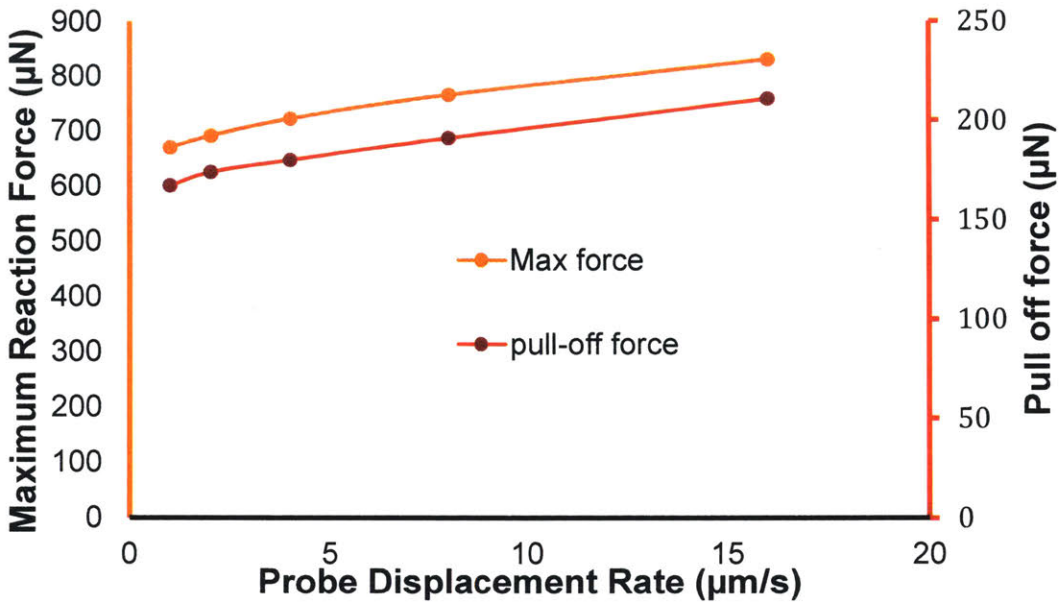

Figure 2-19. Effect of Probe displacement rate on Reaction and Pull Off Force: Illustrates the almost linear effect of probe displacement rate on both reaction and pull off force. Both increase as the probe displacement rate of loading and unloading, respectively, are increased.

2.3.3 Quantifying Hysteresis as a function of the strength of adhesion

An important characteristic in evaluating these models is the degree to which work is dissipated or lost as surface effects become more prominent. To evaluate this, we first define our notation using figure 2.20:

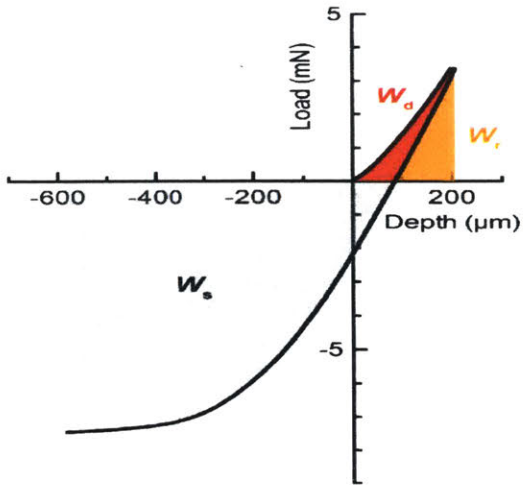

Figure 2-20. Load-depth hysteresis of indentation: This curve shows the notation used to describe our hysteresis analysis. If we consider work input (the area under the loading curve) to reach a final depth as $\boldsymbol{W_t}$, and the work of indentation recovered as the area under the unloading curve $\boldsymbol{W_r}$, then the dissipated work of indentation is $\boldsymbol{W_t - W_r}$. If we consider the initial state as zero force and the returned state as zero force (though at different displacement), $\boldsymbol{W_d}$ represents traditional hysteresis. $\boldsymbol{W_s}$ is then the work of separation. The area under the curve below the x axis represents additional energy input required to cause separation of the probe and sample.

We evaluated the work of dissipation for all simulated cases, including those that did not separate during the simulation. W_d calculated by FEM output (~4-8nJ) was less than that calculated from load-depth profiles of experiments; W_d in experiments was ~8-12nJ for a max force of 800μN and approximate loading rate of 0.05 mN/s (which very roughly corresponds to a probe displacement rate of 4-6 μm/s). The dissipated work of indentation results conducted at loading/unloading rate of 2 μm/s is shown in Figure 2.21.

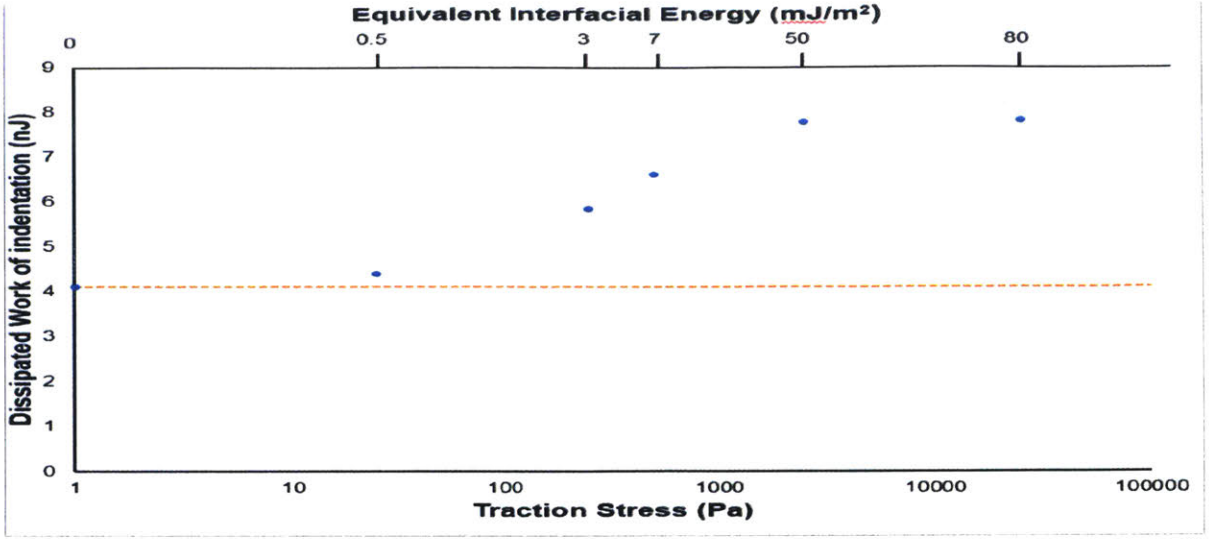

Figure 2-21. Comparison of Dissipated Work of Indentation: This figure shows the non-linear increase from unadhered (represented by the non-adhesive purple dashed line) and completely adhered (represented by the 25000Pa data point) at a strain rate of 2 μm/s.

We then evaluated the work of separation for each model for all simulations that separated fully during the evaluated time. W_s for each model test are included in Figure 2.22 below:

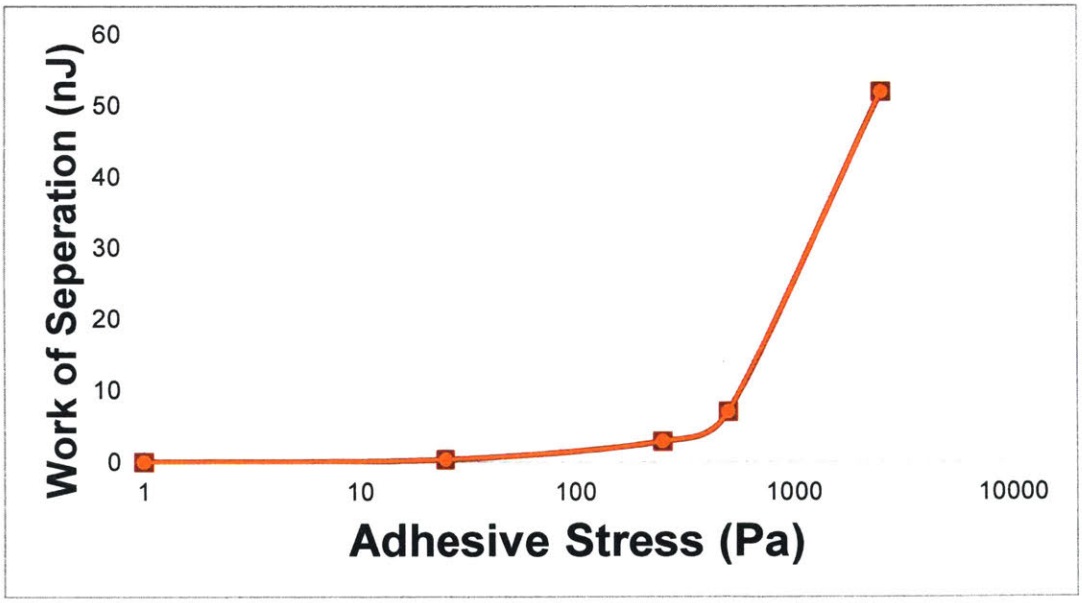

Figure 2-22. Work of Separation: The work of separation grows in proportion to the area of the under the curve as reaction force becomes negative.

Though it is not possible to establish a surface energy referred to in the chapter one discussion of JKR adhesion theory, an approximate interfacial energy, γ_{12}, can be obtained by dividing the work of separation by the area of contact. The area of contact is given by Equation 28 below:

$$A = 2\pi rh \tag{28}$$

Where r is the radius of the sphere and h is the depth of indentation. For the model, each sphere indents to the same depth in all cases, and thus the area of contact is the same, specifically for an 80 μm depth and 2 mm probe radius, the contact area is approximately 1 mm squared. Similarly, though the JKR equations do not account for viscous deformation, we investigated a comparison of these surface energies derived from the maximum pull-off force (discussed in equation 25 in chapter one) to the values of the surface energy derived from the work of separation. This yields approximate interfacial energies for each input traction stress (critical stress of delamination) described in Figure 2.23.

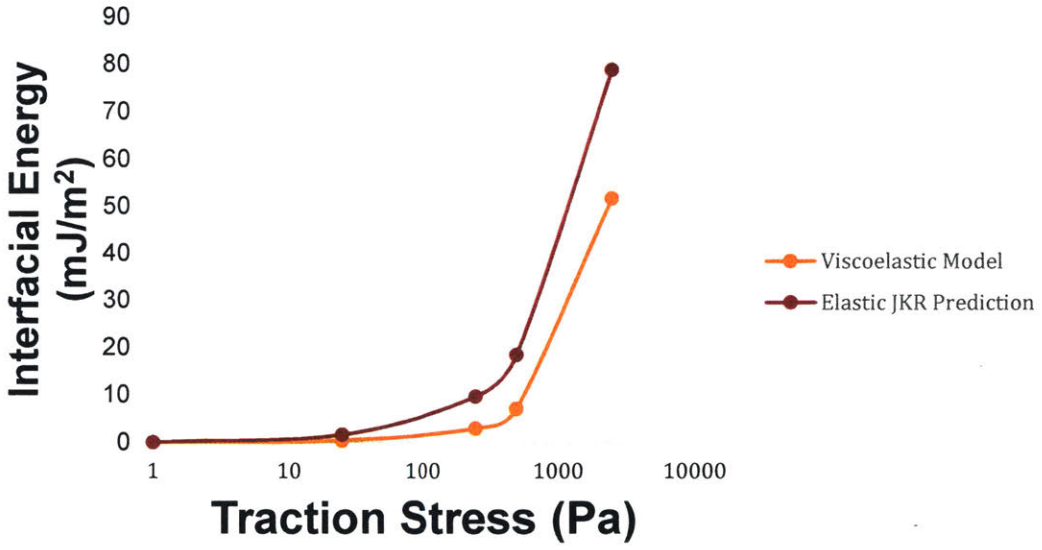

Figure 2-23. Interfacial Energy Comparison: Calculated interfacial energy, γ_{12}, based on work of separation and JKR pull off force.

For reference, surface energy of PDMS is approximately 25mJ/m^2 which corresponds approximately to a traction stress of 1000 Pa if PDMS surface energy dominates the interfacial energy γ_{12}.[41]

2.3.4 Decoupling Adhesion from Viscous Response

One of the stated goals of this finite element model was the ability to decouple the response of the viscous and adhesive component of the polymer as probe displacement rate was varied per Figure 2.18. To do this, we obtained simulation results from all critical traction stresses shown in Figure 2.15, but at a probe displacement rate of 16μm/s instead of 2μm/s. The results of which are shown in figure 2.24 below:

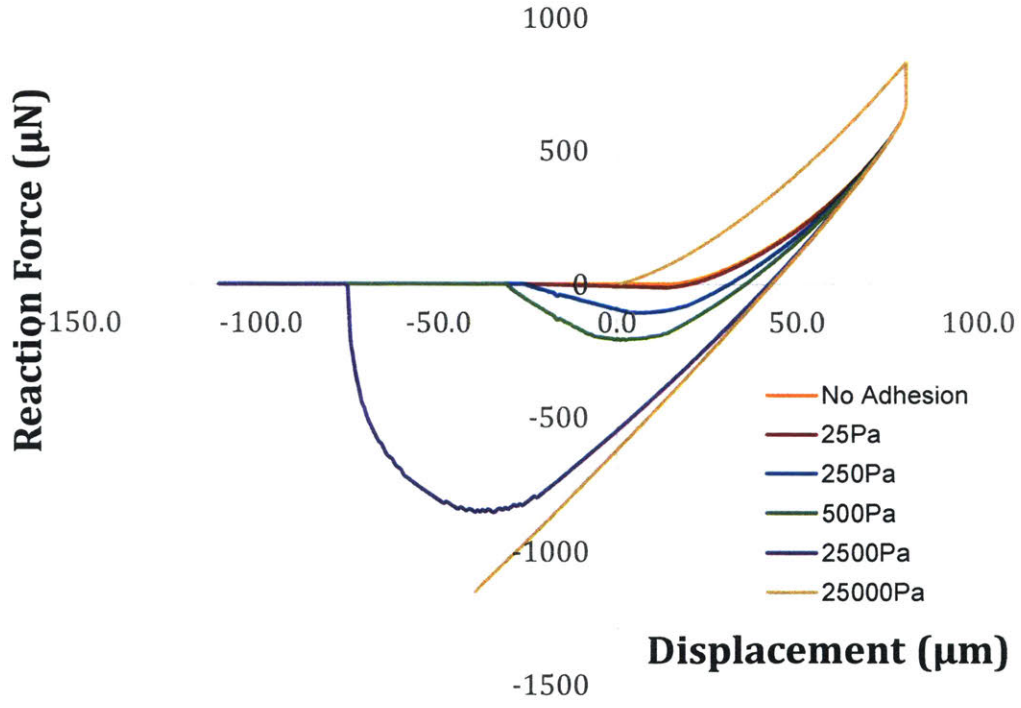

Figure 2-24. Force-Displacement profile at a probe displacement rate of 16μm/s: This figure shows the force displacement profile similar to figure 2-15 above but for a probe displacement rate eight times greater.

Two qualitative trends are immediately apparent, and demonstrated via select comparison of the non-adhesive cases in figure 2-25 below. First, the total work W_t was increased for

increasing probe displacement rate. Second, the recovered work W_r was reduced. Since $W_{t16} > W_{t2}$ and $W_{r16} < W_{r2}$, Wd (the hysteresis equal to $W_t - W_r$) is immediately understood to be greater for the high probe displacement rate case.

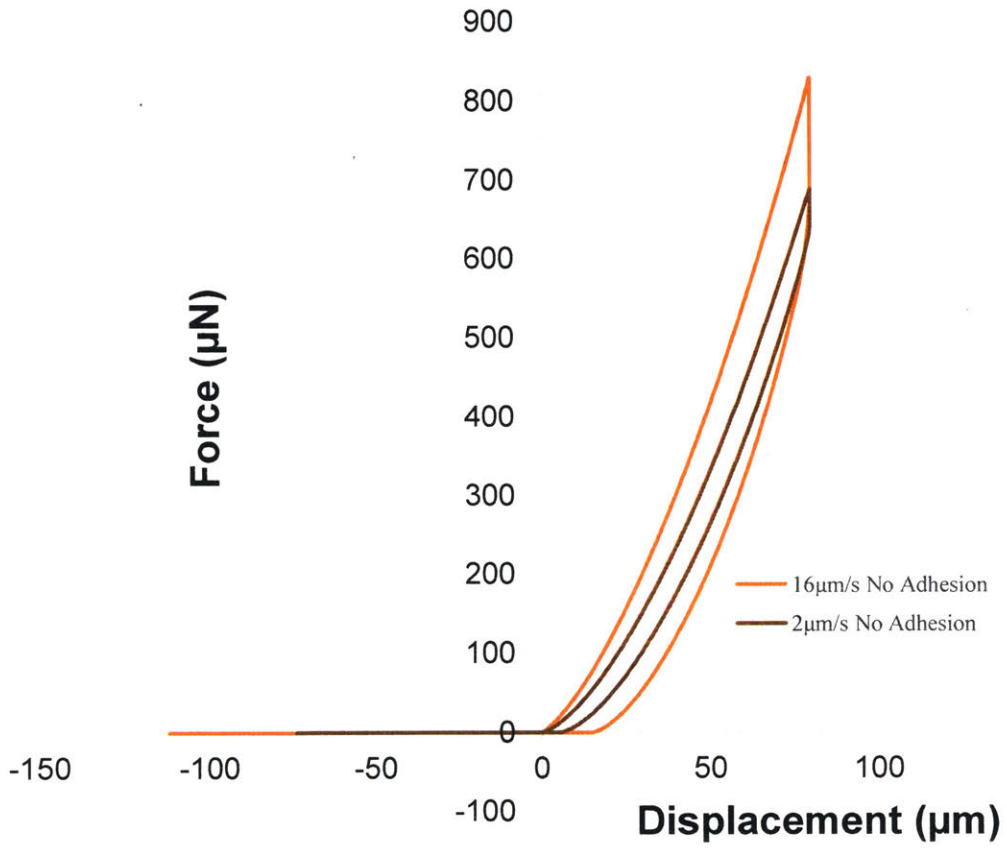

Figure 2-25. Select Comparison between Probe Displacement Rate Responses Without Adhesion: This figure shows that the work input and work recovered in both probe displacement rates of 16μm/s and 2μm/s simulations.

This change in work input and recovery is fully outlined in Figure 2.26.

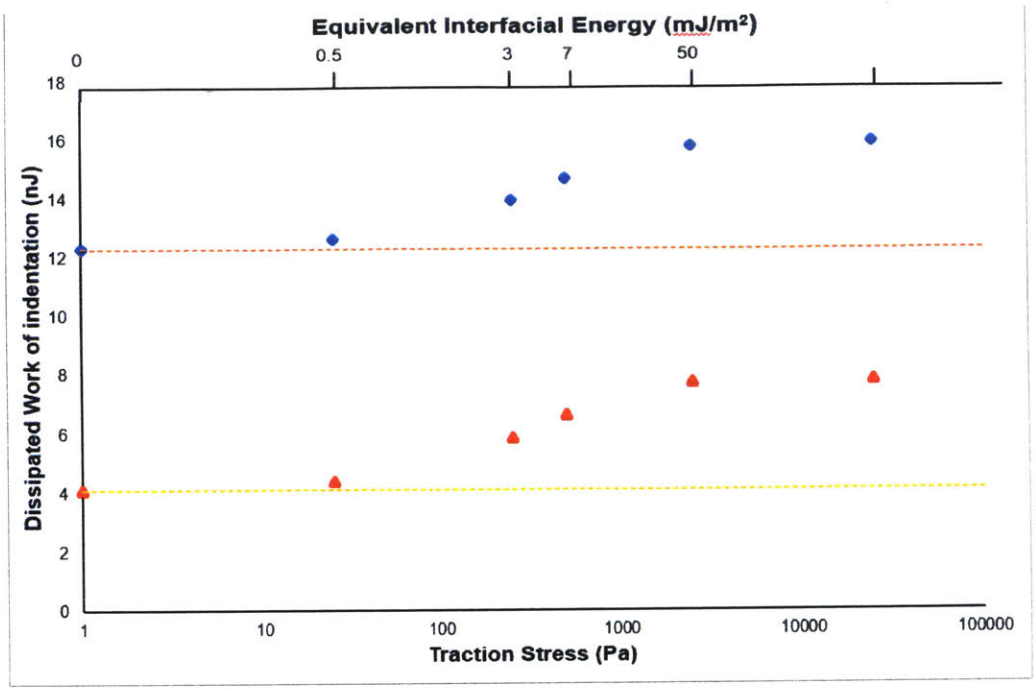

Figure 2-26. Dissipated Work of Indentation Comparison: This figure shows that the dissipated work of indentation W_d at 2μm/s and 16μm/s. The dashed orange and red lines represent non-adhesive cases at those respective probe displacement rates.

Figure 2-26 shows that W_d or dissipated work increased significantly, (approximately by a factor of 3) for increased displacement rate (factor of 8). At both the higher and lower displacement rates, increased adhesion (increased traction stress and corresponding γ_{12}) increased W_d. Since no other variables are changing, we conclude that the $\Delta W_d = W_d - W_d(\gamma_o)$, or the change in work of dissipation is equal to the observed work of dissipation for each γ_{12} minus the work in the non-adhesive case. We see from figure 2.26, that change in work of dissipation due to adhesion for the most adhesive trials (25000Pa or ~80 mJ/m^2) at both high and low indentation rates increased the dissipated work by the same ~3.6nJ. That means that on a percentage basis, highlighted in Table 2.2 below, adhesion plays a stronger role at lower displacement rates contributing 47% of the dissipated response at 2μm/s and 22% of the dissipated response at 16μm/s at the same traction stress (25000Pa). Since adhesive contributions were independent of the probe displacement rate, we predict that at very low probe displacement rates the dissipated work due to adhesion should dominate over the dissipated work due to the

viscoelastic properties of the polymer. To evaluate this, more work must be done to determine what loading profile would give a fully adhesion dominated response.

Table 2.2: Comparison of Dissipated Work and Strain Rate at Variable Traction Stress

Traction Stress (Pa)	Probe Rate (μm/s)	Wt (nJ)	Wr (nJ)	Wd (nJ)	ΔWd(nJ)	Adhesion %
25000	16	26.95743508	11.05315328	15.9042818	3.604128803	22.66137414
25000	2	21.62600245	13.82138144	7.804621013	3.672399473	47.05416787
2500	16	26.95743508	11.1924944	15.76494068	3.464787683	21.97780349
2500	2	21.62600245	13.87709762	7.748904833	3.616683293	46.67347672
500	16	26.95743508	12.2805094	14.67692568	2.376772683	16.19394098
500	2	21.62600245	15.01894061	6.607061847	2.474840307	37.45750175
250	16	26.95743508	12.99274204	13.96469304	1.664540043	11.91963216
250	2	21.62600245	15.78339225	5.842610199	1.710388659	29.27439279
25	16	26.95743508	14.35115942	12.60627566	0.306122667	2.428335497
25	2	21.62600245	17.23178056	4.394221895	0.262000355	5.962383367
0	16	26.95743508	14.65728208	12.300153	0	0
0	2	21.62600245	17.49378091	4.13222154	0	0

2.3.5 Limits of the model

Every computational model has specific limitations to the effectiveness or range of applicability. In this case, we investigated the maximum pull-off force that we could achieve with the model. After highly refining the mesh, and greatly decreasing timestep involved, we found that the maximum pull-off force that we could achieve with the model was 2.98 mN. Unlike most simulations we evaluated, at this high pull-off force we observed increasing mesh distortion, and finally model completion failure as excessive displacement causes necking to occur in the material to the point at which some elements in contact were excessively distorted.

While most experimental samples exhibited pull-off forces, less than or equal to 3 mN, our most adhesive experimental CY-52 polymer sample had a maximum pull-off force greater than 5mN. To expand the model to cover our most adhesive experimental cases we tried many fixes to overcome this model deficiency. The first was implementing non-linear adaptive meshing (NLAM). This is an ANSYS subsystem implemented in the command section that

dynamically refines mesh elements that become excessively distorted as the simulation continues. However, NLAM is a relatively recent addition to the ANSYS architecture, and does not support cohesive zone boundaries; thus after a few iterations, the model began displaying incoherent and disjointed reaction forces and this approach was discarded. A second approach, currently being investigated, is manual mesh rezoning via command console at a specific load step. This requires writing commands to suspend the simulation, redraw the mesh zones under high strain, overlay the stress and strain data from the old mesh to the new mesh and restarting the simulation after processing. At the time of this writing, this approach has not been successfully implemented because of the technical complexity.

2.3.6 Conclusions

In this chapter, we explored the role of adhesion, the effect of increasing displacement rate and quantified the work lost due to both adhesive and viscous properties of the polymer. Previously, running indentation experiments allowed us to characterize the mechanical response of polymers and tissue simulants, but this adhesion model allows us to decouple the adhesive and viscous responses on the work of dissipation. Upon analyzing the results of this model, we conclude that although dissipated work is increased by increasing strain rate, that dissipated work is not affected by the strength of adhesion. This leads to the prediction that at both very fast and very slow timescales of indentation, at timescales at which viscous effects are negligible, adhesion should dominate the materials response observed.

3 HIGH VELOCITY PARTICLE IMPACT MODELLING

3.1 Poly(urethane urea) Case Study

While modelling adhesive effects are important to the understanding of material responses at long timescales or low velocities, for impact approaching ballistic shockwave velocities we must also consider shorter timescales of response. To accomplish this, we switch from implicit to explicit finite element modelling, and thus the timescale of our modelling changes from hundreds of seconds to hundredths of a second. This chapter presents two case that illustrate key methods necessary for a high velocity projectile impact model and the usefulness and limitations of these models. The first case study is of Poly(urethane urea), a stiff, glassy elastomer used to demonstrate the process of building a high velocity model. The second case study is of gelatin, described in chapter one, and investigated for potential applicability in simulating tissue response. In both cases, simulation results are designed and compared with unique particle impact experiments developed by Keith Nelson and David Veysset at MIT as part of an ISN project team led by Van Vliet.

3.1.1 Poly(urethane urea) Microstructure and Properties

High performance ballistic glass that is simultaneously lightweight, transparent, and able to resist perforation by projectiles is highly sought in aviation, defence and military applications. To be effective in most applications, ballistic glass must be mechanically hard, energy absorbent, and durable. Conventional ballistic glass has utilized a glass-polycarbonate construction for which protection varied based upon the thickness of the glass.[42] While effective, this resulted in increasingly heavy plates reaching 3.5 inches in width to provide protection against a wide range of ballistic threats. While recent incorporation of a hard front layer of transparent ceramics such as aluminum oxytrinide,[43] and magnesium aluminate spinel[44] have reduced the overall weight of ballistic glass designs, new ballistic materials are still highly desired for more rigorous applications. Various materials have been suggested and tested, including ultrahigh molecular

weight polyethylene composites,[45] and various epoxy-composite structures, but this section is focused on the modelling of poly(urethane urea) or PUU.

PUU is a segmented block copolymer already notable for its variable molecular weight "soft" block and its current use in biomedical applications. PUU has three blocks or components: 1,6-hexamethylene diisocyanate (HMDI), and diethylenetriamine (DETA) hard blocks, and variable poly(tretramethylene oxide) (PTMO) soft block.[46] The length of the PTMO segment has a dramatic effect on the mechanical properties of the material. The shorter the PTMO segment, the more uniform the material and hence the more uniform the resulting mechanical properties of the resulting PUU are. The greater the ratio of hard to soft mole of precursors used, the greater the stiffness of the resulting PUU. Thus, PUU are often given named designations such as PUU 2:1:1-2000 which would correspond to 2 mol PTMO with a molecular weight of 2000g/mol, combined with one mol HDMI, and DETA. The structure of PUU is detailed in figure 3.1 below:

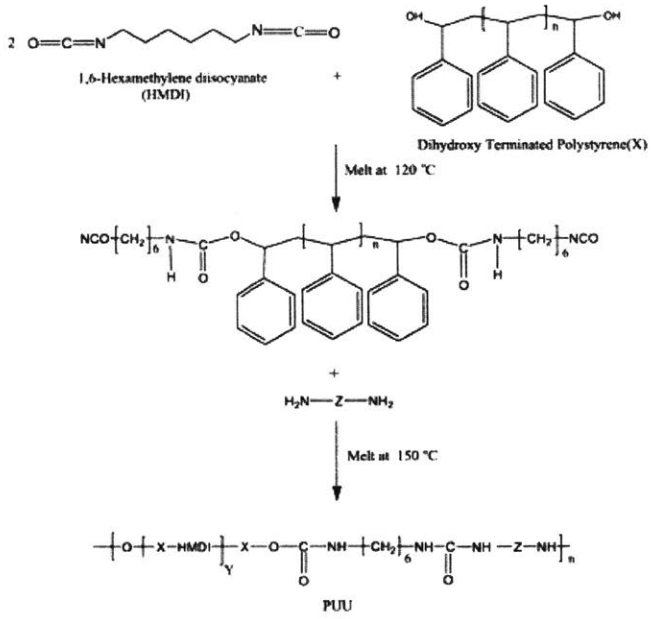

Figure 3-1. PUU Formulation: This figure shows how PUU is formulated and how the material can be tuned to a stiffer or more compliant formulation (From Strawhecker et al.[47])

Due to the varied nature and formulation of PUU copolymers, few formulations have complete materials data such as shear or viscoelastic data. However, with a few experimental tests, enough materials properties can be obtained to create a reasonably approximate simulation. While it would be possible to simply test PUU plates in a ballistic environment, without simulations, the cost prompts the creation of simulations that can help predict material response without the need to bring materials to a ballistics range or iterate empirical production test cycles.

3.1.2 Calculated Materials Properties

Creating an accurate simulation requires accurate input material properties. While this case study focuses on PUU 5:3:2-1000, some material properties are approximated via comparisons to similar PUU formulations and, as indicated similar polyurea copolymers. Using data provided by Dr. Alex Hsieh (ARL and ISN), the density and longitudinal wave speed of this particular PUU sample were known (1090 kg/m^3 and 1640 m/s).[47] U.S. Navy investigations of PUU indicated that the shear wavespeed of a given PUU polymer were roughly 20% of the longitudinal wavespeed (330 m/s).[48] The shear wave speed (C_s) can be expressed as the wave equation:

$$C_s = \sqrt{\frac{\mu}{\rho}} \tag{29}$$

Where μ is the shear modulus and ρ is the density, while also knowing the longitudinal wavespeed:

$$C_l = \sqrt{\frac{M}{\rho}} \tag{30}$$

Where the wave modulus M is:

$$M = 2\mu + \lambda \tag{31}$$

and λ is Lame's first parameter.

Three homogeneous isotropic linear elastic conversion formulas can be applied in sequence relating Lame's first parameter:

$$\lambda = \rho * C_l{}^2 - 2\rho * C_s{}^2 \quad (32)$$

To the bulk modulus:

$$K = \lambda + \frac{2}{3} * \mu \quad (33)$$

Which yields the Young's modulus:

$$E = \frac{9K(K-\lambda)}{3K-\lambda} \quad (34)$$

The Young's modulus can be analyzed for consistency by analyzing the resultant Poisson ratio given by:

$$v = \frac{\lambda}{3K-\lambda} \quad (35)$$

In this case the PUU sample exhibited a v of 0.47, which is very close to the expected 0.5 of an incompressible solid. Deriving the shear modulus from these values, in this case Go = 120 MPa, is necessary to the construction of the shock model described in Equation 14 (chapter 1) and explored in the next section.

3.1.3 Derived Shock Data

As discussed in chapter one, shock data can be derived from by knowing just the initial density, the shock velocity and the particle velocity. The initial density is easily recovered leaving only the particle and shock velocity to be determined. To retrieve this information, we review the experiment conducted by the U.S. Army Research Laboratory on PUU 5:3:2-1000 by

Casem and Hsieh.[49] To calculate the shock properties of PUU a high velocity, Soda Lime Glass (SLG) impact test was conducted by those researchers.

In an SLG test, depicted in Figure 3.2 below, a cylindrical slab of material of interest (in this case PUU) is fired at high speeds into a cylindrical sheet of target material that is held in place by fixed supports. The target material is selected to remain perfectly elastic throughout the entire duration of the test, even at high impact speeds. The material in this test is Soda Lime Glass, a very stiff material. Using Velocity Interferometer System for Any Reflector (VISAR) feedback, the position of the free surface, and hence the velocity, (referred to as u_1 in Equations 5 through 11 in chapter 1) can be determined.

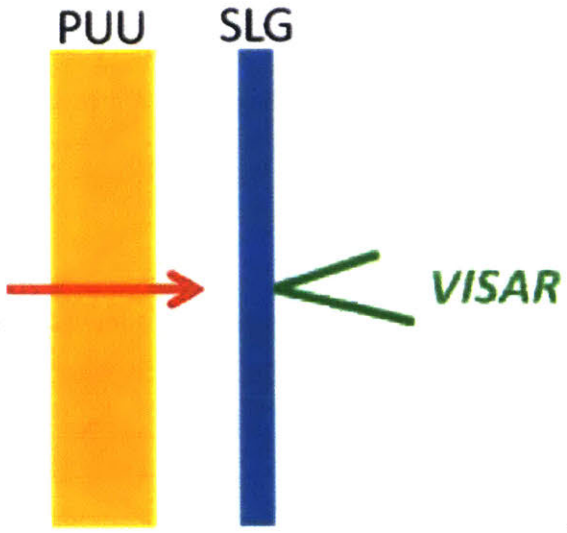

Figure 3-2. SLG Test Setup: This figure shows how an SLG test for shock is conducted. (From Casem et al).[49]

Using a highspeed camera, the shock speed of the material can be observed for all time points of the free surface. Since the SLG unloads in steps based on the shock of the material (depicted in Figure 3.3), multiple particle velocities may be extracted to correspond to shock speeds.

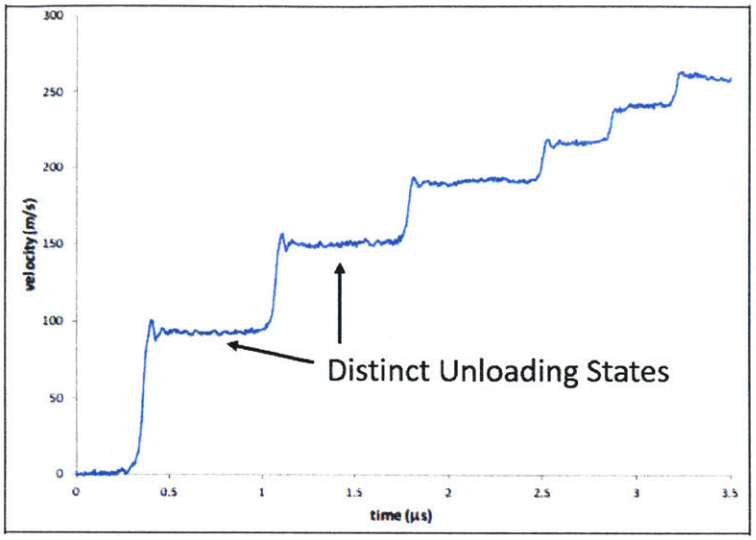

Figure 3-3. SLG VISAR Response at 298m/s impact: This figure shows the velocity of the free surface of the glass during the unloading process. (Figure adapted from Casem et al.)[49]

Analyzing images from the high speed camera data and using Equations 8, 9 and 10, the particle speed and shock speed were calculated by Dr. Hsieh for each distinct unloading state, to then obtain the density of the shocked material. The unloading states with shock speed of U_S and particle speed U_P are shown in Table 3.1.

Table 3.1: Distinct Unloading States of Soda Lime Glass at 298 m/s

Step No.	Density (kg/m^3)	Strain	Stress (GPa)	U_S (m/s)	U_P (m/s)
0	1061	0	0.000	NA	0
1	1179	0.099812	0.672	2519	251
2	1148	0.076111	0.417	3119	176
3	1124	0.056339	0.288	2461	127
4	1110	0.043767	0.194	2638	94

Using a second impact test on PUU at a velocity of 1000 m/s a stress-strain relationship can be determined and is shown below in figure 3.4:

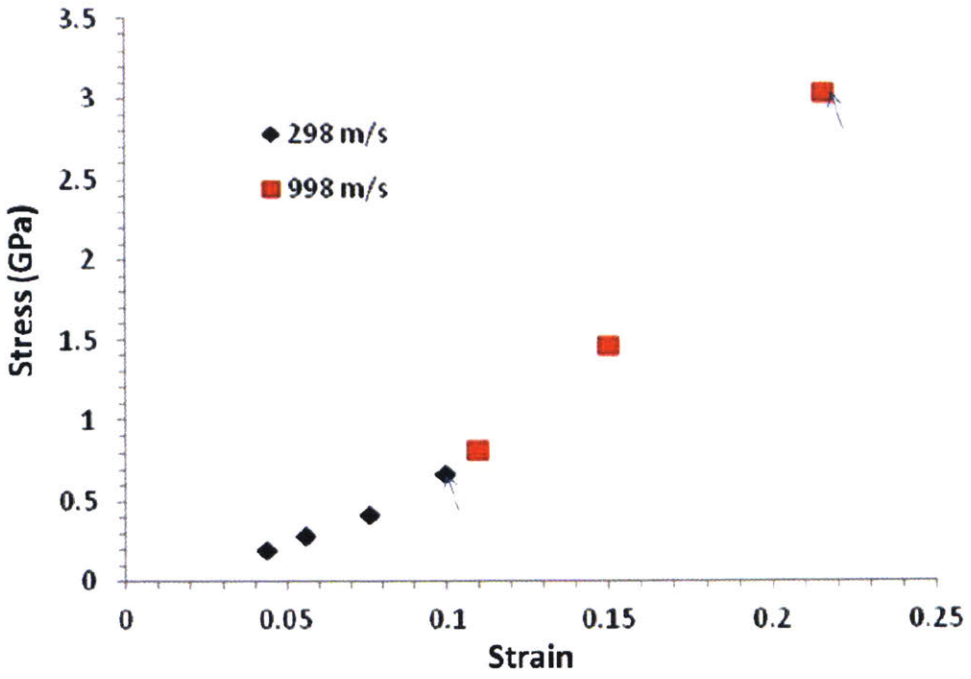

Figure 3-4. Stress Vs Strain for Distinct Unloading States: This graph shows the stress strain derived from table 3.1 and its equivalent 998m/s table showing the stress strain relationships at distinct unloading states. (From Casem et al).[49]

Feeding this information back into equation 12 we obtain a shock equation of state of the form stated in equation 11. This linear shock equation of state is depicted in Figure 3.5:

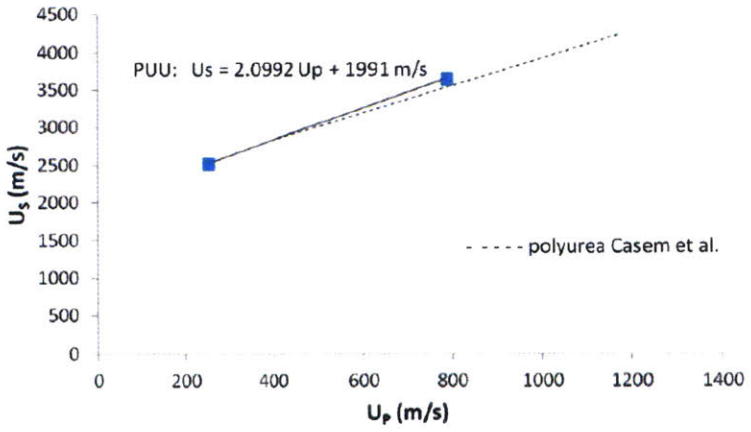

Figure 3-5. Particle Speed versus Shock Speed of PUU 532-1000: Here, shock versus particle speeds for the material are compared to the well documented shock equation of state for polyurea, a similar material. (From Casem et al).[49]

The Grunesien coefficient was not investigated in the study, so to finalize the Mei- Grunesien equation of state, the coefficient was borrowed from polyurea (1.5). We are assuming elastic

linear shock, so while two points is the minimum to get a relationship between shock and particle velocity, it should be sufficient for modelling purposes. Further, the comparison to the shock equation of state for a closely related, but better characterized material polyurea suggests that the equation of state should be close to, if not perfectly aligned with the true shock equation of state of polyurethane urea.

3.1.4 Experimental Setup

The experimental setup for high velocity impact tests that served as motivation for our FEM is shown in Figure 3.6. Summarizing the experimental procedure described in Veysset et al.[50] A laser excitation pulse was focused onto a launching pad assembly from where solid micron-sized silica spheres, of diameter seven micron, were ejected. Upon laser ablation of the gold film, particles were accelerated to speeds ranging from 200 m/s to 1500 m/s controllable via adjustments to the laser excitation. For each test, 16 images were recorded with a high frame rate camera (SIMX, Specialized Imaging) using a laser pulse for illumination. Each image was recorded independently with exposure times as short as 3 ns. Using the independently triggered imaging system, a highly precise instantaneous projectile velocity could be recorded for all time points of each experiment. This experimental approach is called LIPIT by the authors, or Laser Induced Projectile Impact Test.

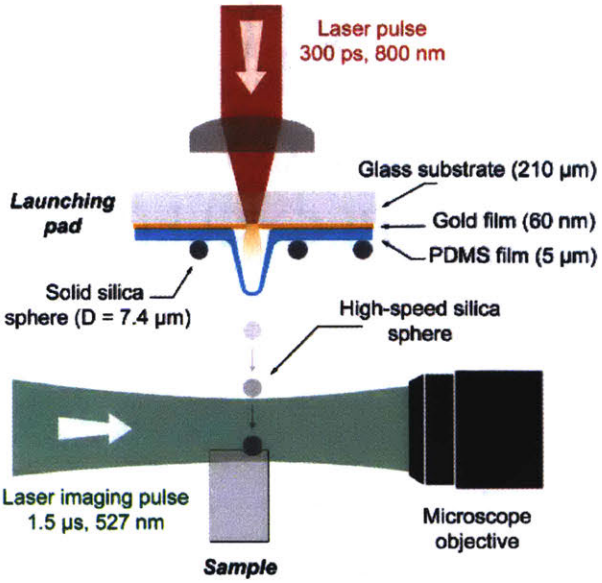

Figure 3-6. Particle Launch and Imaging Configuration: Upon laser ablation of the gold film, the PDMS layer expands and ejects the silica spheres at speeds up to 1500m/s. The sample is positioned approximately 1 mm away from the launching pad. The microsphere is aimed to hit the sample near the edge facing the microscope objective. (From Veysset et al.)[50]

3.1.5 Finite Element Model Setup

To recreate the dimensions of this experiment, a two dimensional, axisymmetric model was created. The model consists of two bodies, a rigid, fused silica spherical particle (impactor) and a plate of PUU constrained at the base. As compared to the impactor, the plate is three diameters wide and four diameters deep, and is divided into three segments of one, one and two diameters in depth, of decreasing mesh density as shown in Figure 3.7.

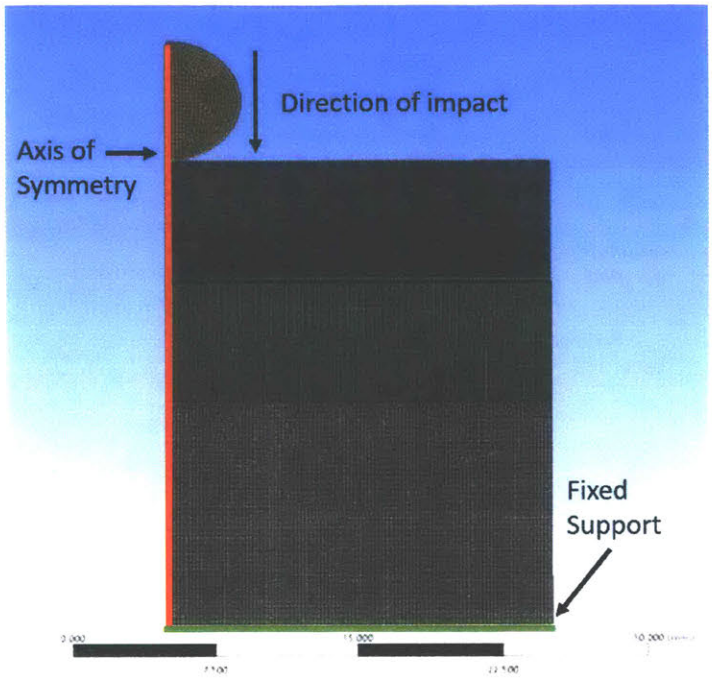

Figure 3-7. Finite Element Model Setup: This figure shows the setup designed to capture the experimental setup described in section 3.1.4. Frictionless contact is enforced throughout the duration of the simulation. 2D axisymmetry significantly shortens computational time. A fixed support at the base of the elastomer prevents movement away as the force from the indenter is applied. The spherical impactor is assigned the properties of fused silica, and imparted an initial velocity.

To avoid complications arising from very small element areas caused from meshing at or below an aspect length of 1 μm (which can result in zero area elements) the model was scaled from the micro meter scale to the millimeter scale. Scaling laws indicate that normalized depth of penetration, normalized energy dissipation and shock responses should not change based on the change in length scale. Instead, the only thing that should change is timescale of response.

To ensure that our mesh size was adequate to ensure accurate response, we conducted a mesh convergence study at 500 m/s depicted in Figure 3.8. The optimized variable is the coefficient of restitution e, which, defined, is the rebound velocity normalized by the initial velocity of the impactor.

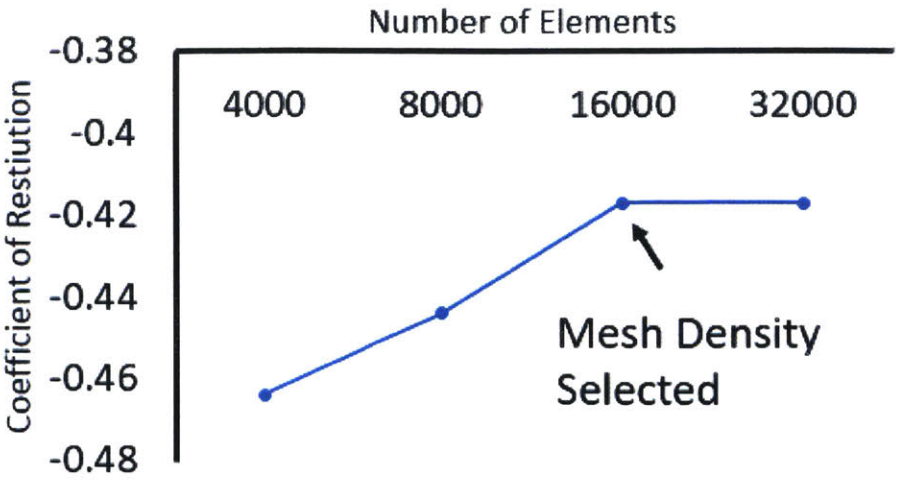

Figure 3-8. Mesh Convergence Study for PUU at 500m/s: The mesh size chosen was 16000 elements. There was no change in the coefficient of restitution after the increasing the density to 32000 elements.

3.1.6 Model Comparison

The impact profile (with timescale normalized to account for length scaling) is compared at 500m/s in figure 3.9 below. The model was then varied from 100m/s to 700m/s and compared to experimental data derived from LIPIT experiments as in Figure 3.9:

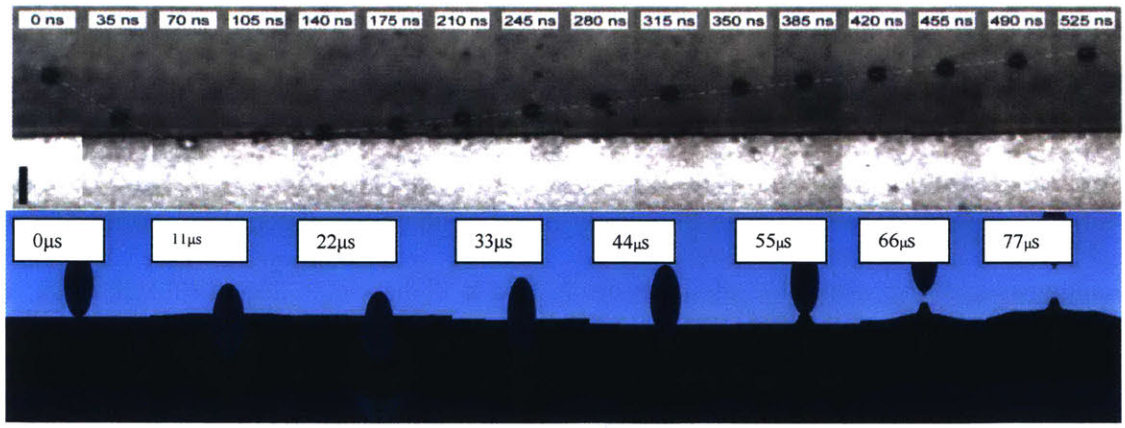

Figure 3-9. Impact Profile Comparison: This figure shows the impact profile at equivalent speed in both FEM and experimental models. The approximated time of contact for the experiment is 75ns before rebound and a scaled 70 μs for the model.

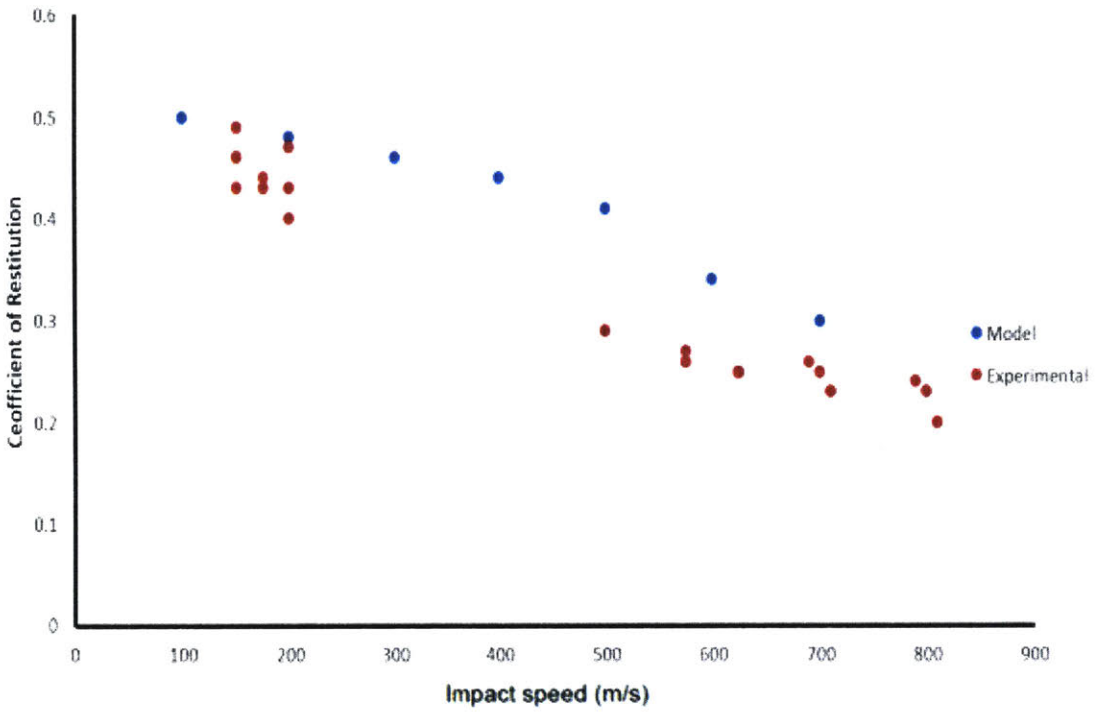

Figure 3-10. Coefficient of Restitution Comparison: In this figure we show the comparison between the FEM model and the experimental data on PUU 532-1000.

Figure 3.10 shows the final result of the investigation into shock using the FEM model described above. While the data is not a perfect fit for the experimental LIPIT results, the model shows similar qualitative trends with those data. Namely, a fairly linear trend over the range of impact speeds conducted by both LIPIT and FEM testing with increasing energy dissipation (denoted by decreasing e as the velocity was increased). While the model cannot decouple the exact effects of shock, the change in the purely linear trend of the material at around 500m/s likely suggests and increasing role of shock dissipation at higher velocities. In future work, an investigation of the effect of varying temperature on impact response would be valuable for the expansion of the model since experimental data on PUU impact since data (shown in Figure 3.11) suggest that increasing temperature can alter the energy dissipation of the material without a change in the shock equation of state (but rather through the Mie-Gruneisen coefficient discussed in chapter 1).

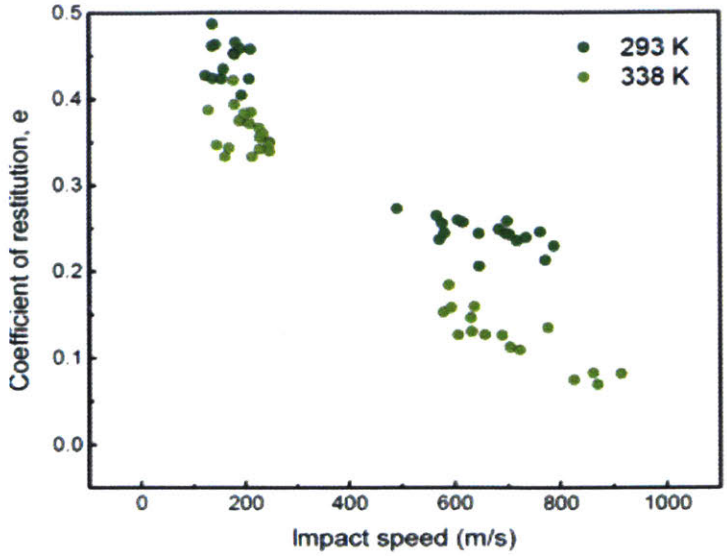

Figure 3-11. Temperature/Impact Study of PUU 532-1000: Here we see the effects of temperature on PUU 532 response. (Adapted from Veysset et al).[50] As temperature is increased the coefficient of restitution of the impactor is reduced indicating additional energy dissipation.

3.1.7 Model Expansion (Polycarbonate)

The PUU case study was designed to show how a shock equation of state can be derived and implemented in an ANSYS simulation. Continuing the investigation of shock related responses, we briefly investigated the effect of turning off shock in a well known material, polycarbonate, whose isotropic and shock equation of state are contained within ANSYS sample materials. Though this study is still in its infancy, several key facets of the model are being investigated such as the effect of changing the slope of the materials Rayleigh line (see Figure 1.8), changing the effective speed of sound of the material (which would affect the v shock effects) and the effect of removing shock from the model.

Of these, only the comparison between shock enabled and shock disabled polycarbonate have been investigated and the results are included in Figure 3-12.

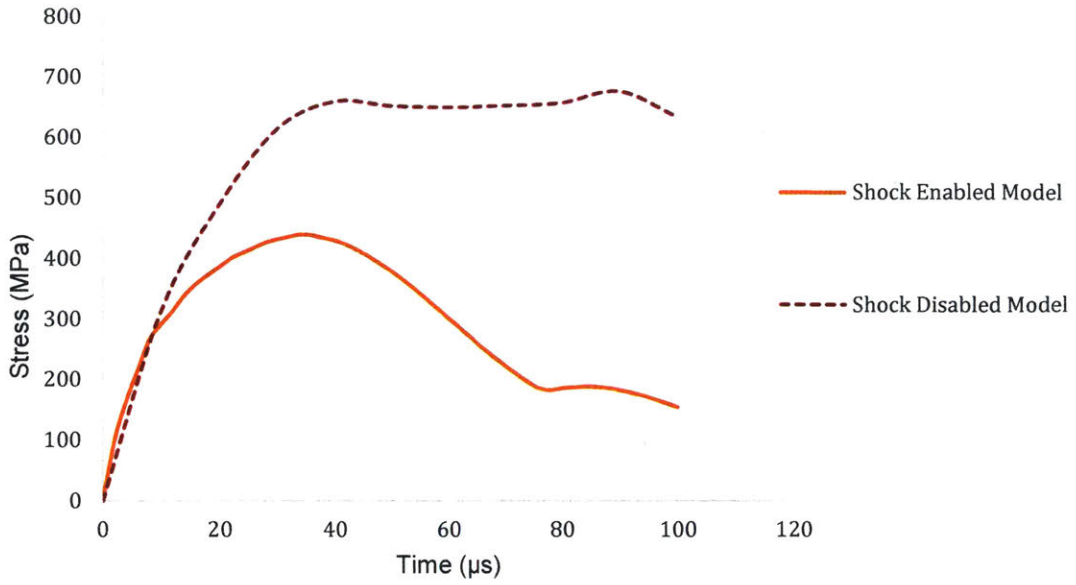

Figure 3-12. Comparison of Shock Enabled and Shock Disabled Models: This figure shows the equivalent stress experienced by the polycarbonate model during impactat 500 m/s. The shock enabled model was shown to dissipate energy more easily and results in a lower maximum stress experienced during an impact event at 430 MPa. The shock disabled model resulted in a maximum stress of 660 MPa and over the timescale of the impact event was much high for much longer.

Figure 3.12 shows very simply the apparent stress response of the polycarbonate when shock loading is both enabled and disabled as that is the only difference between the models. Initially, both materials share the same approximate loading curve subject to the elastic properties of the material, but the shock enabled model appears to dissipate energy more easily and more quickly from impact, while the shock disabled model has both a higher maximum and higher average stress during the timescale of loading. Work was not finished to investigate this phenomenon further, but this study indicates that shock loading likely plays a significant role in energy dissipation at high impact speeds.

Ultimately, we did not investigate the PUU or polycarbonate model further since the goal of this project was to investigate hydrogels, tissues and tissue simulants at high speed. To do this, we switched our investigation to gelatin.

3.2 Gelatin Case Study

3.2.1 Gelatin Microscale Structure and Properties

The physical makeup of gelatin and how that microscale structure corresponds to a desirable, tunable tissue simulant for testing were discussed in section 1.1.2.

3.2.2 Literature Materials Properties

Unlike poly(urethane urea) which has sparse materials properties in literature, gelatin has been a highly investigate material since the 1950s. However, due to the varied and heterogeneous nature as discussed in chapter one, and various methods of material property characterization, it was difficult to find consensus on a number of mechanical properties. Table 3.2 below provides a brief summary of material properties from prior studies. The table includes the percent gelatin tested, the measured shear modulus, the density and the slope S and intersect of the shock C equations as per form of equation 11.

Table 3.2: Literature Values for Gelatin Material Properties

Author	Vol. % Gelatin	Shear Modulus G_o (MPa)	Density (kg/m^3)	S	C (m/s)
Nagayama[51]	20	N/A	1060	2	1560
Amador[52]	15	0.00537	1050	N/A	N/A
Swain[53]	15	10.1	1050	N/A	N/A
Amador[52]	10	0.00357	1030	N/A	N/A
Czerner[54]	10	0.0133	1080	N/A	N/A
Swain[53]	10	6.67	1030	N/A	N/A
Nagayama[51]	10	N/A	1030	2	1520

Yoon[55]	10	0.217	1030	1.93	1553
Swain[53]	7.5	3.95	1020	N/A	N/A
Amador[52]	7	0.00161	1015	N/A	N/A
Swain[53]	5	2.17	1010	N/A	N/A

As shown in the table, consistent evaluation of gelatin is very difficult to obtain, however for our purposes, we will use the approximate shear moduli from Swain et al (for gelatin formulations of 5 to 15%), and the approximate linear shock equation of Nagayama et al. We conducted impact tests over a range of theoretical shear modulus values from 1 to 10 MPa. We also incorporated the shock equation of state expressed in both Nagayama and Yoon's shock studies to compare results.

3.2.3 Finite Element Model Architecture

Initially, the model was constructed as a two-dimensional axisymmetric setup identical to the model discussed in section 3.1.5. However, due to the excessive strain rates on a material model relatively low stiffness, this two-dimensional axisymmetric model was extremely unstable and not useful in generating consistent data, due to the propensity of nodes to fail and energy loss error to accumulate as the velocity of impact was increased. In ANSYS explicit simulations, energy loss greater than 10% indicates that the simulation results are suspect at best and worthless at worst. For low velocities of 300-500 m/s our simulations exhibited energy loss of up to 20% which was far too great to consider an acceptable solution.

To address this shortcoming of the 2D FEM model, we adopted a planar-symmetric 3D model architecture shown in Figure 3.13. That model enabled the use of the built-in materials failure features of ANSYS Autodyn. The model was still scaled to avoid errors in mesh volume to a 1000X scale of the impact setup described in Figure 3.1.4, but once again this should only

effect the timescale of the impact, not the normalized depth of penetration or other materials responses. From Yoon et al, we defined all five Johnson and Cook failure parameters discussed in Equation 17 in chapter 1 and linked that failure method into the existing model. Once material failure was incorporated into the model, the excessive energy loss due to node failure was eliminated and the simulation generated consistent results.

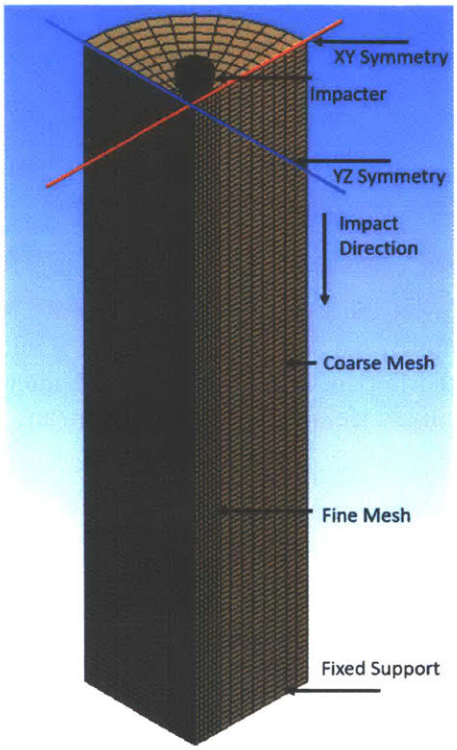

Figure 3-13. Gelatin Impact Model: This figure shows the 3D model setup for measuring the impact of silica projectiles on Gelatin meshes. The model uses the planar symmetry tool (across the XY and YZ planes) to reduce computational load and increase accuracy of the model. The mesh is refined within 1.5 diameters of the impacting projectile all along the axis of impact. The cylinder is 25 impactor diameters deep and 7 diameters across to minimize edge effects without sacrificing model focus.

To test the accuracy of the model, a mesh convergence test for depth of penetration (normalized to the diameter of the projectile) was conducted and shown in Figure 3.14.

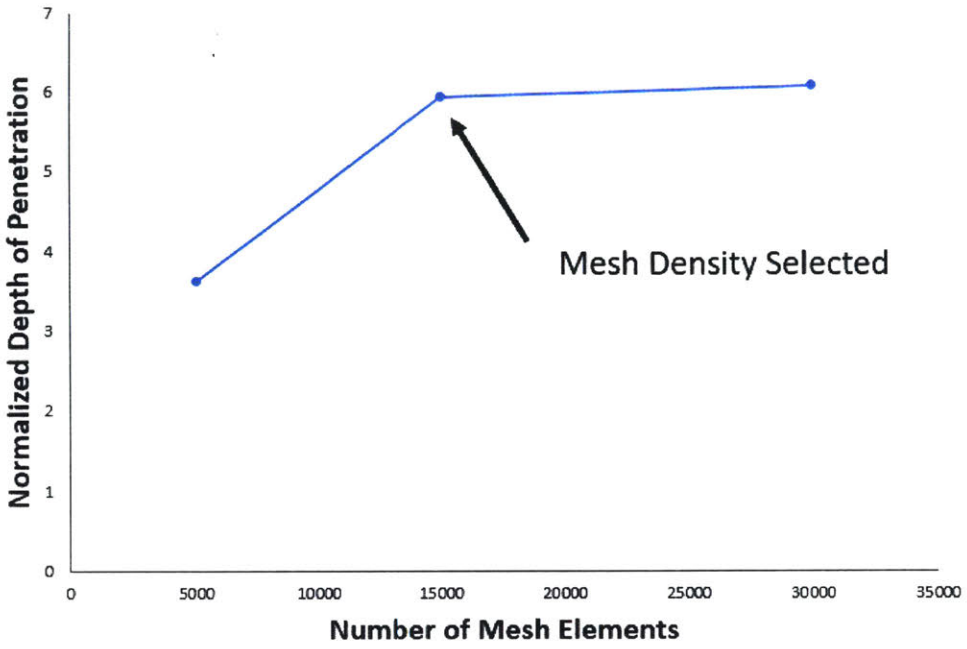

Figure 3-14. Mesh Convergence Study: This figure shows the mesh convergence study conducted using a shear modulus of 6.6 MPa and an initial velocity of 500 m/s to determine an appropriate mesh density for the impact tests. The 16,000 element model was selected on this basis for further trials. Normalized depth of penetration means the depth achieved over the diameter of the indentor.

3.2.4 Model Comparison

Impact data was acquired by D. Veysset et al., using the same LIPIT approach described in section 3.1.4. These data were obtained for gelatin gels of 2.5, 5 and 10% by volume gelatin and used as a basis of comparison for the model as shown in Figure 3.15.

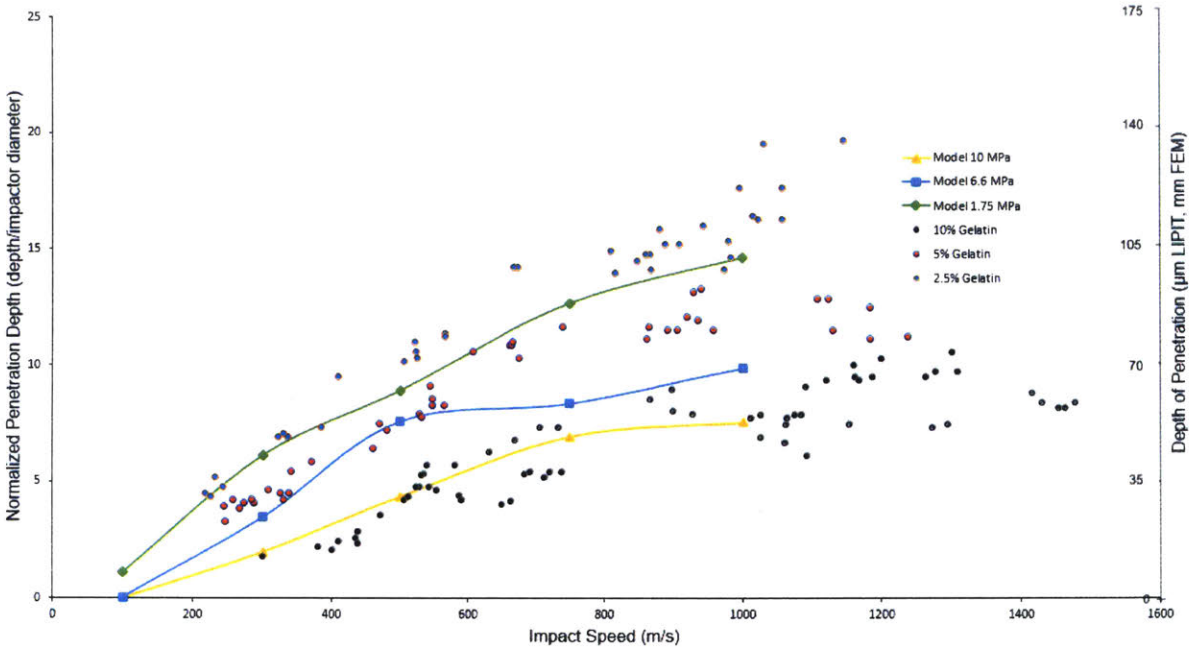

Figure 3-15. Experimental versus FEM Model Comparison: This figure shows the experimental data obtained via Laser Excitation Pulse impacts on Gelatin as described in section 3.1.4 compared to the FEM model using values for shear modulus G_o of 1.75, 6.6 and 10 MPa using the same impactor geometry and material.

While we do not know the actual value of shear modulus for these gelatin samples, if we assume the same order of magnitude stiffness values of Swain et al. (whose impact study represents the closest comparison with LIPIT to the gelatin gel examined experimentally at MIT with LIPIT),[53] the model shows adequate, comparable results to the experimental data.

Specifically, the experimental data for 2.5% gelatin are reasonably well fit by our FEM output that assumed G_o = 1.75 MPa, over the impact velocity range of 200 to 1000 m/s. Likewise, LIPIT experiments for 10% gelatin show penetration depths that agreed reasonably well by those predicted by our FEM model assuming G_o = 10 MPa. This magnitude of shear modulus are similar to mean values obtained by Swain et al. Via shear rheology (6.7 MPa for 10% gelatin), and G_o measured by Swain et al. for 5% gelatin (>2.5%) was 2.2 MPa. Thus we can use our model to estimate what G_o of the gels tested via LIPIT must be, with reasonable confidence. That validated model can next be used to predict penetration depths for new gels of

known G_0 or other impactor geometries and impact speeds. Additionally, the profile of impact resembles the same pattern, a wide temporary cavity formed during the movement of the projectile, through the sample that rapidly collapses back, closing the gap shown below in Figure 3.16.

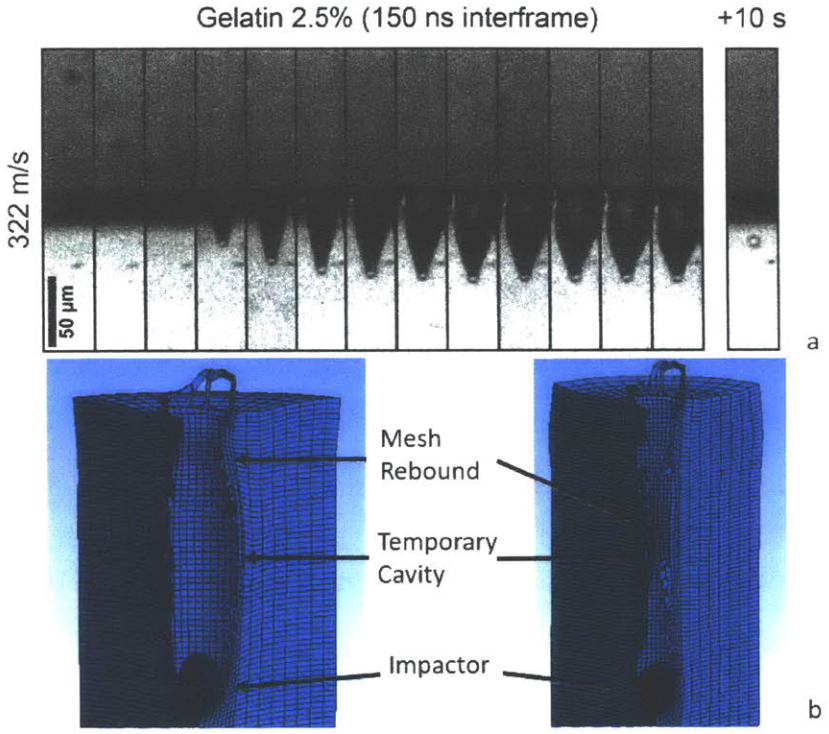

Figure 3-16. Impact Profile: This figure shows the (a) impact profile generated in Veysset et al.'s experimental 2.5% gelatin and (b) FEM G_0 1.75 MPa. In a, we can see the lip of the impact profile beginning to collapse when the end of the high speed monitoring occurs. In b, we see a defined temporary cavity that collapses on itself as the simulation finishes. This phenomenon of temporary cavity with a diameter greater than the diameter of the projectile is a common and still being investigated event in high velocity impacts, especially in compliant materials. This cavity formation and collapse pattern is consistent with cavity formation demonstrated in other high speed impact studies of gelatin.[55]

While a full study on the diameter of the temporary cavity created during the simulation has not been completed, qualitatively, Figure 3.16 demonstrates the formation and collapse of the feature common in high velocity impact events.

3.3 Model Limitations

Currently both models are limited by the speed at which impact takes place. As velocity increases, the effects of shock loading and the deformation inherent in modelling also increase. This increases the error loss and thus decreases the accuracy of the model as velocity increases. While the velocities studied in these simulations are stable, increasing the velocity still higher will compound the effect of these errors and certainly limit the useful range of the model. Materials failure data is a useful tool in combating the onset of energy error, but even this approach has distinct limits. Further mesh refinements and forcing ANSYS to proceed at a slower timesteps to avoid energy loss are acceptable ways of pushing the limits of the model, however, forcing the model to use arbitrarily low timesteps can increase the computational cost by orders of magnitude and without an ANSYS Autodyne license (provided by DRAPER) the limit of refinement for those seeking to replicate this study is 32000 nodes provided by the free student license. Some thought was given to the incorporation of adhesion, the relative role of surface effects in high velocity impact such as this, we predict that adhesion would likely play a minor role, if any at all. Further, the differences between the explicit and implicit ANSYS software prevent a direct implementation of the adhesion as it was described in chapter 2 and would have to be initiated as a new effort.

4 SUMMARY AND FUTURE WORK

The purpose of this thesis was to construct and validate two finite element model types, each with differing mechanical constitutive laws and impact conditions, to provide a framework for testing and evaluating tissues and polymers computationally. The first model replicated the effects of adhesive contact over a large range of simulated interfacial energies of the polymer, while the second model allows for the investigation of projectile impact and shock on stiff and compliant polymers (idealized as elastic) over a large range of initial kinetic energies. The limits of each model were explored but the potential uses of each model have not been investigated in full depth.

The first model can be used to decouple the effect of adhesion on load-indentation depth hystereses at quasi-static loading conditions from other properties including viscoelastic constants and constitutive laws, can investigate the response of bilayer gels, and can simulate responses of novel simulants with minimum required experimental data. The second model can be used primarily to measure the bulk response of simulants and tissues arising from high velocity (m/s) particle impact. The effective temperature can be altered via mechanical property inputs to investigate impact at various thermal conditions, such as at body temperature, or material impact data can be fitted to make a determination of the approximate shock or shear conditions present, or mechanical properties inferred via forward or inverse analysis of depth-time profiles.

Ultimately, the uses of each model have not been fully explored, but the models themselves stand as a tested framework for future research. Further work can use such models for designing and refining new protective strategies against blunt and penetrative injuries, and for understanding hierarchical design of biological or synthetic polymers for mechanical energy dissipation .

5 REFERENCES

1. Wade, A. L., Dye, J. L., Mohrle, C. R. & Galarneau, M. R. Head, face, and neck injuries during Operation Iraqi Freedom II: results from the US Navy-Marine Corps Combat Trauma Registry. *J. Trauma* **63,** 836–840 (2007).

2. Mijailovic, A. S. Methods to Measure and Relate the Viscoelastic Properties of Brain Tissue. (Massachusetts Institute of Technology, 2016).

3. DoD. *Department of the Army the Army. 7-22.7* **7,** (2002).

4. Nester, C. J. Lessons from dynamic cadaver and invasive bone pin studies: do we know how the foot really moves during gait? *J. Foot Ankle Res.* **2,** 18 (2009).

5. Granville, L. Anatomy Cadaver as a ' First Patient ' Experience. *MedEdPortal Publ.* **10,** 9975 (2014).

6. Snedeker, J. G. *et al.* Strain-rate dependent material properties of the porcine and human kidney capsule. *J. Biomech.* **38,** 1011–1021 (2005).

7. Shirahama, H., Lee, B. H., Tan, L. P. & Cho, N.-J. Precise Tuning of Facile One-Pot Gelatin Methacryloyl (GelMA) Synthesis. *Sci. Rep.* **6,** 31036 (2016).

8. Appleby-Thomas, G. J. *et al.* On the dynamic behavior of three readily available soft tissue simulants. *J. Appl. Phys.* **109,** 1–6 (2011).

9. Shepherd, C. J., Appleby-Thomas, G. J., Wilgeroth, J. M., Hazell, P. J. & Allsop, D. F. On the response of ballistic soap to one-dimensional shock loading. *Int. J. Impact Eng.* **38,** 981–988 (2011).

10. Lazebnik, M., Madsen, E. L., Frank, G. R. & Hagness, S. C. Tissue-mimicking phantom materials for narrowband and ultrawideband microwave applications. *Phys. Med. Biol* **50,** 4245–4258 (2005).

11. Moy, P. & Weerasooriya, T. Dynamic response of an alternative tissue simulant, physically associating gels (PAG). *Proc. Soc. Exp. Mech. Conf.* (2006).

12. Zhang, T. *et al.* Synthesis, properties of fullerene-containing polyurethane-urea and its optical limiting absorption. *Polymer (Guildf).* **44,** 2647–2654 (2003).

13. Elzoghby, A. O. Gelatin-based nanoparticles as drug and gene delivery systems: Reviewing three decades of research. *J. Control. Release* **172,** 1075–1091 (2013).

14. Duconseille, A., Astruc, T., Quintana, N., Meersman, F. & Sante-Lhoutellier, V. Gelatin structure and composition linked to hard capsule dissolution: A review. *Food Hydrocoll.* **43,** 360–376 (2015).

15. Murphy, M. Decreased Brain Stiffness in Alzheimer's Disease Determined by Magnetic Resonance Elastography. *J Magn Reson Imaging* **34,** 494–498 (2011).

16. Mrozek, R. A., Cole, P. J., Otim, K. J., Shull, K. R. & Lenhart, J. L. Influence of solvent size on the mechanical properties and rheology of polydimethylsiloxane-based polymeric gels. *Polymer (Guildf).* **52,** 3422–3430 (2011).

17. Kalcioglu, Z. I. *et al.* Tunable mechanical behavior of synthetic organogels as biofidelic tissue simulants. *J. Biomech.* **46,** 1583–1591 (2013).

18. Chatelin, S., Constantinesco, A. & Willinger, R. Fifty years of brain tissue mechanical testing: From in vitro to in vivo investigations. *Biorheology* **47,** 255–276 (2010).

19. Demkowicz, M. J. Effect of symmetry on elastic response. **10,** 109–121

20. Gasser, T. C., Ogden, R. W. & Holzapfel, G. A. Hyperelastic modelling of arterial layers with distributed collagen fibre orientations. *J. R. Soc. Interface* **3,** 15–35 (2006).

21. Asay, J. R. & Shahinpoor, M. Equation of State. *High-Pressure Shock Compression of Solids* 75–113 (1993). doi:10.1007/978-1-4612-0911-9_4

22. ANSYS Inc. ANSYS Mechanical User's Guide. *ANSYS Manual* **16.2,** https://www.sharcnet.ca/Software/Ansys/16.2.3/en-u (2014).

23. Gordeyev, Y. N. Growth of a crack produced by hydraulic fracture in a poroelastic medium. *Int. J. Rock Mech. Min. Sci.* **30,** 233–238 (1993).

24. Prasad, A., Dao, M. & Suresh, S. Steady-state frictional sliding contact on surfaces of plastically graded materials. *Acta Mater.* **57,** 511–524 (2009).

25. Liu, Y., Paulino, G. H. & Liang, L. Elasto-viscoplastic consistent tangent operator concept-based implicit boundary element methods. *Sci. China Ser. E Technol.* **43,** 154–164 (2000).

26. Banerjee, A., Dhar, S., Acharyya, S., Datta, D. & Nayak, N. Determination of Johnson cook material and failure model constants and numerical modelling of Charpy impact test of armour steel. *Mater. Sci. Eng. A* **640,** 200–209 (2015).

27. Zhu, X., Siamantouras, E., Liu, K. K. & Liu, X. Determination of work of adhesion of biological cell under AFM bead indentation. *J. Mech. Behav. Biomed. Mater.* **56,** 77–86 (2016).

28. Kumaran. in *Fundamentals of Rheology* 1–46 (Indian Institute of Science, 2009).

29. Zimberlin, J. a., Sanabria-DeLong, N., Tew, G. N. & Crosby, A. J. Cavitation rheology for soft materials. *Soft Matter* **3,** 763 (2007).

30. Lomakina, E. B., Spillmann, C. M., King, M. R. & Waugh, R. E. Rheological analysis and measurement of neutrophil indentation. *Biophys. J.* **87,** 4246–58 (2004).

31. Canovic, E. P. *et al.* Characterizing multiscale mechanical properties of brain tissue using atomic force microscopy, impact indentation, and rheometry. *J. Vis. Exp.* **2016,** 1–12 (2016).

32. Pacheco, J. E. L., Bavastri, C. A. & Pereira, J. T. Viscoelastic relaxation modulus characterization using Prony series. *Lat. Am. J. Solids Struct.* **12,** 420–445 (2015).

33. Qing, B. & Van Vliet, K. J. Hierarchical design of synthetic gel composites optimized to mimic the impact energy dissipation response of brain tissue. *Mol. Syst. Des. Eng.* **1,** 290–300 (2016).

34. You, H. Finite Element Method. **2,** 1–4 (2003).

35. Kanit, T., Forest, S., Galliet, I., Mounoury, V. & Jeulin, D. Determination of the size of the representative volume element for random composites: Statistical and numerical approach. *Int. J. Solids Struct.* **40,** 3647–3679 (2003).

36. Shan, Z. & Gokhale, A. M. Representative volume element for non-uniform micro-structure. *Comput. Mater. Sci.* **24,** 361–379 (2002).

37. Zacher, B. & Armstrong, N. R. Modeling the effects of molecular length scale electrode heterogeneity in organic solar cells. *J. Phys. Chem. C* **115,** 25496–25507 (2011).

38. Bjorkman, G. S. *et al.* Mesh convergence studies for thin shell elements. *ASME 2011 Press. Vessel. Pip. Conf.* 119–123 (2011).

39. Miller, E. Writing and Compiling a Custom Material Property in ANSYS Mechanical APDL. 1–57 (2012).

40. Meng, J. *et al.* Effect of strain rate on adhesion strength of Anisotropic Conductive Film (ACF) joints. *2013 IEEE 63rd Electron. Components Technol. Conf.* 1252–1258 (2013). doi:10.1109/ECTC.2013.6575735

41. Geiser, M., Schurch, S. & Gehr, P. Influence of surface chemistry and topography of particles on their immersion into the lung's surface-lining layer. *J. Appl. Physiol.* **94,** 1793–1801 (2003).

42. Straßburger, E. Ballistic testing of transparent armour ceramics. *J. Eur. Ceram. Soc.* **29,** 267–273 (2009).

43. Zhang, J. J. Transparent Glass-Ceramic Armor. **1,** 1–8 (2007).

44. Reimanis, I. E., Kleebe, H.-J. & Cook, R. L. Transparent Spinel Fabricated from Novel Powders: Synthesis, Microstructure and Optical Properties. *Def. Secur. Symp.* 9 (2004).

45. Hsieh, A. J., Chantawansri, T. L., Hu, W., Cain, J. & Yu, J. H. New insight into the influence of molecular dynamics of matrix elastomers on ballistic impact deformation in UHMWPE composites. *Polym. (United Kingdom)* **95,** 52–61 (2016).

46. Xu, R. & Manias, E. New Biomedical Poly(urethane urea)-Layered Silicate Nanocomposites. *Macromolecules* 337–339 (2001). doi:10.1021/ma0013657

47. Strawhecker, K. E., Hsieh, A. J., Chantawansri, T. L., Kalcioglu, Z. I. & Van Vliet, K. J. Influence of microstructure on micro-/nano-mechanical measurements of select model transparent poly(urethane urea) elastomers. *Polym. (United Kingdom)* **54,** 901–908 (2013).

48. Ramotowski, T. & Jenne, K. NUWC XP-1 polyurethane-urea: A new, 'acoustically transparent' encapsulant for underwater transducers and hydrophones. *Ocean. 2003 Celebr. Past... Teaming Towar. Futur.* **1,** 227–230 (2003).

49. Casem, D. T. & Hsieh, A. J. Plate-Impact Measurements of a Select Model Poly (urethane urea) Elastomer. (2013).

50. Veysset, D. *et al.* Dynamics of supersonic microparticle impact on elastomers revealed by real–time multi–frame imaging. *Sci. Rep.* **6,** 25577 (2016).

51. Nagayama, K., Mori, Y., Motegi, Y. & Nakahara, M. Shock hugoniot for biological materials. *Shock Waves* **15,** 267–275 (2006).

52. Amador, C., Badalà, F., Nouri-mahdavi, K. & Raoof, D. A. Shear elastic modulus estimation from indentation and SDUV on gelatin Phantoms. *IEEE Trans Biomed Eng* **58,** 724–732 (2011).

53. Swain, M. V., Kieser, D. C., Shah, S. & Kieser, J. A. Projectile penetration into ballistic gelatin. *J. Mech. Behav. Biomed. Mater.* **29,** 385–392 (2014).

54. Czerner, M., Fellay, L. S., Suárez, M. P., Frontini, P. M. & Fasce, L. A. Determination of Elastic Modulus of Gelatin Gels by Indentation Experiments. *Procedia Mater. Sci.* **8,** 287–296 (2015).

55. Yoon, G. H., Mo, J. S., Kim, K. H., Yoon, C. H. & Lim, N. H. Investigation of bullet penetration in ballistic gelatin via finite element simulation and experiment. *J. Mech. Sci. Technol.* **29,** 3747–3759 (2015).

6 APPENDICES

6.1.1 Matlab Code for Rheology Data

This code was used to convert shear rheology data from CY52 PDMS obtained by Bo Qing and Alex Mijailovic into instantaneous and infinite shear moduli, and Prony series components necessary for the construction of the authors Finite Element Models. Direct output of the code can be found in chapter 2, Figures 2.2 and 2.3.

For the CY52 samples considered in this thesis, the table below summarizes the composition and extracted prony series parameters generated via this code:

Table 6.1.1: Prony Series Components of CY52 used in Chapter 2

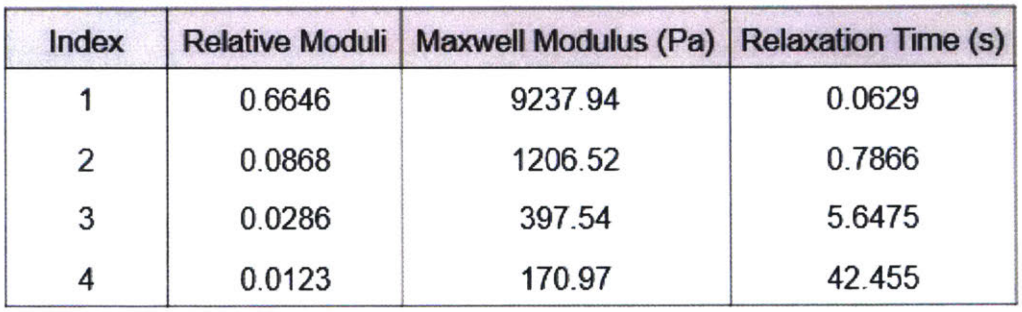

Index	Relative Moduli	Maxwell Modulus (Pa)	Relaxation Time (s)
1	0.6646	9237.94	0.0629
2	0.0868	1206.52	0.7866
3	0.0286	397.54	5.6475
4	0.0123	170.97	42.455

```
%%%%%%%%%%%%%%%%%%%%%%%%%%%%%%%%%%%%%%%%%%%%%
%  Modified by Alex Mijailovic and Kyle
Geiser 10/21/16     %
% (Mostly written by Aarthy/Roza)           %
%%%%%%%%%%%%%%%%%%%%%%%%%%%%%%%%%%%%%%%%%%%%%
clc
clear all
close all

global freq G_strg_exp G_loss_exp tau x0 G0
PronyLength
data=xlsread('Rheology_CY52andSE.xlsx');
 % load experimental data
freq = data(28:67,4); % frequency in Hz
```

```
G_strg_exp = data(28:67,5); % storage modulus
in Pa
G_loss_exp = data(28:67,6); % loss modulus in
Pa

% Plot storage modulus
StorageM = figure('Name','Storage Modulus');
loglog(freq, G_strg_exp,'ro'); hold on;
ylabel('Storage Modulus(Pa)');
xlabel('Frequency (Hz)');
% Plot loss modulus
LossM = figure('Name','Loss Modulus');
loglog(freq, G_loss_exp,'ro'); hold on;
ylabel('Loss Modulus(Pa)');
xlabel('Frequency (Hz)');
% Plot loss modulus
BothM = figure('Name','Modulus');
loglog(freq, G_loss_exp,'ro'); hold on;
ylabel('G'' G''''(Pa)');
xlabel('Frequency (Hz)');


n = length(freq); % number of fitting points
G_strg = zeros(1,n);
G_loss = zeros(1,n);

Ginf = min(G_strg_exp) % shear modulus,
initial assumption
PronyLength = 4; % Max length of Prony series
Matrix = zeros(PronyLength,PronyLength+3);
N=PronyLength;
% for N = 1:PronyLength
    tau = logspace(min(freq),max(freq),N); %
generate relaxation times

    % Initial guess from lsqnonlin without
constraint sum(gi)<1
```

```
    g = rand(1,N);
    g = g/sum(g); % Prony series parameters,
initial assumption
    x0 = [G0, g,tau]; % variables to be
optimized
    lb =
[0,zeros(1,N),1/max(freq)*ones(1,N)]; % lower
bounds for variables
    ub =
[10^8,ones(1,N),1/min(freq)*ones(1,N)]; %
upper bounds for variables
    [x,resnorm] = lsqnonlin(@calc3,x0,lb,ub);
%lsqnonlin minimizes squared sum of vectors
from calc3
x=x';
%make prony data a matrix
%structure
%G0 Ginf
%g1 t1
%g2 t2
%...
%gN tN
PronyData=[x(1), x(1)*(1-
sum(x(2:N+1)));x(2:N+1), x(N+2:end)];

gi=x(2:PronyLength+1);
taui=x(PronyLength+2:end);
for j=1:n
    G_strg(j) = x(1)*(1-sum(gi)+
sum(gi.*taui.^2*freq(j)^2./(1+taui.^2*freq(j)
^2)));
    G_loss(j) =
x(1)*sum((gi.*taui*freq(j)./(1+taui.^2*freq(j
)^2)));
end
```

```
% Plot to compare with experimental storage
modulus
figure(StorageM)
loglog(freq, G_strg,'kd');hold on
% Plot to compare with experimental loss
modulus
figure(LossM)
loglog(freq, G_loss,'kd');hold on
%plot to compare both
figure(BothM)
loglog(freq, G_strg,'kd');hold on
loglog(freq, G_loss,'kd');hold on

csvwrite('PronySeries.txt', PronyData);
%structure of this text file
%G0 Ginf
%g1 t1
%g2 t2
%...
%gN tN
```

6.1.2 Model Sample Input File

A sample input file is several hundred pages long. An example input file is archived in a stored location described below in section 6.1.4.

6.1.3 Model Sample Output File

A sample output file is several hundred pages long. An example input file is archived in a stored location described below in section 6.1.4.

6.1.4 Stored Locations for all Models

All copies of the model are stored on the L Drive, Toshiba external hard-drive, Model: HDWC130XK3J1, SN: 359KVASGSU17 under the file folder: E:\Permanent ANSYS FILES.

The files used to generate the data for chapter 2 are located as workbench files: AdhesionNew2, StrainRateStudy, and FlatPunchStudy located under the file folder: **E:\Permanent ANSYS FILES\Current**. The data parsed from those files are located in the same directory under excel files, strainratestudy and adhesionstrengthstudy.

The files used in chapter 3 section 1 are located in: **E:\Permanent ANSYS FILES\Ansys Files**. The workbench file, file axi_working_steel_2 and its excel counterpart are the file location and data parsing files. The files used in chapter 3 section 2 are located in **E:\Permanent ANSYS FILES\Current**. The workbench file is titled gelatin_copy and the excel file for data parsing are located in the excel file Gelatin_Impact_data_Thesis_mod.

Sample Input and Output Files are stored under the headers: Sample_Input and Sample_Output located in **E:\Permanent ANSYS FILES\Current**. All files and folders, including test files and test cases are also saved to dropbox to ensure files are not accidentally lost or misplaced.

6.1.5 Sample Calculation of Interfacial Energy γ_{12} from Traction Stress

Referring back to Figure 2.20, we consider that the energy required for separation is equal to the total area under the curve after the probe displacement is returned to zero during unloading. Using Euler's method of integration to calculate the area under the force-displacement curve for each timestep, W_s can be calculated for all simulations that fully seperate. For each traction stress at 2μm/s that W_s in nJ was displayed in figure 2.22.

We also know that this work of separation acts over the defined area of contact between indenter and polymer. Since our radius and depth of penetration were set as part of the model setup, it becomes easy to calculate the area of sphere in contact with a half plane, given by equation 28 in chapter 2.

$$A = 2\pi rh \tag{28}$$

Dividing the known work of separation by the area of contact gives our approximate interfacial energy described in figure 2.23. Thus our measured response gives a relationship between interfacial energy and traction stress used to model adhesion in this thesis.

6.1.6 Comparison of FEM Particle Impact Simulations with Analytical Models

Often, it's useful to compare the results of a computational model to the expected results using an analytical model. In this thesis, a primitive version of the indentation model was compared to expected results of Hertz contact and found near perfect agreement. This comparison was useful to validate the model, but provides little novel information about mechanical processes. High velocity impact on the other hand does not have a defined analytical model, but is sometimes compared to fluid flow models such as the Bingham model of plastic flow.

A Bingham plastic is a material that shows no deformation to applied stress until a critical yield stress is reached and the material behaves as a viscous material. This is similar to the description of sliding frictional elements given in chapter 1. An analytical model, known as the Poncelet model uses the governing equations for a Bingham plastic to predict penetration depth based on a coefficient of drag and a material yield stress, which are related to a material's "resistivity." The author of this thesis did not work extensively with this model and so the equations are not presented, but did compare his results to those determined by yield stress fitted by David Veysset shown in figure 6.1.

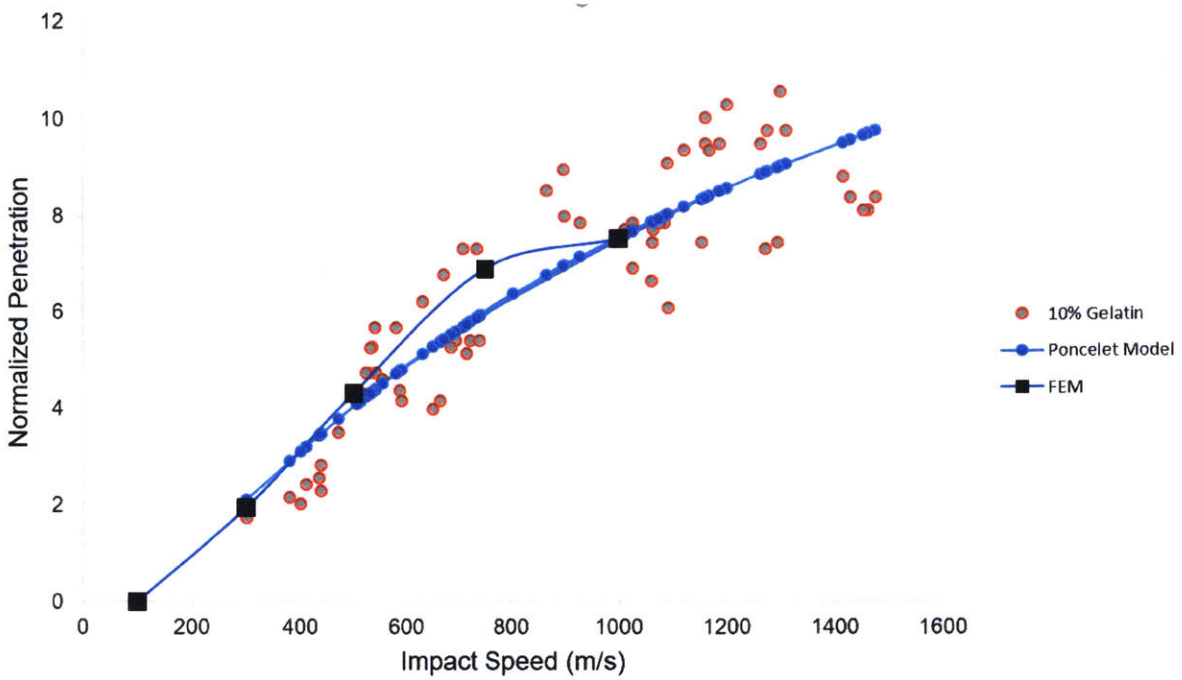

Figure 6-1. Comparison of 10% Gelatin, fitted Poncelet model from D. Veysset and FEM model of the author: This figure shows the similarities of the FEM model, whose constitutive law describes the gelatin as elastic, but capable of shock loading and material failure. The Poncelet model is fitted to the data using a known coefficient of drag, allowing the model determine a yield stress.

As we see in Figure 6.1, the Poncelet model and the FEM model have remarkably good agreement, however there is no constitutive reason for this to be the case. The FEM model response is primarily based on the shear modulus input. The Poncelet model doesn't account for shear modulus at all. The author believes that the similarity in trend is a natural product of the fitting process of the Poncelet model. Since one key constitutive property can freely vary the model will always have a minimum least squares regression. Had the Poncelet model been based on an experimental yield stress this comparison may be more useful, but still as enigmatic since the constitutive models are not similar. This dissimilarity in model governing equations while retaining similarity in results presents an interesting avenue for future exploration of the model.